Thermochemical effects on hypersonic shock waves interacting with weak turbulence

C. Huete, A. Cuadra, M. Vera, and J. Urzay

COLLECTIONS

F   This paper was selected as Featured

View Online   Export Citation   CrossMark

Thermochemical effects on hypersonic shock waves interacting with weak turbulence ⓕ

C. Huete,[1,a] ⓘD A. Cuadra,[1] ⓘD M. Vera,[1] ⓘD and J. Urzay[2] ⓘD

AFFILIATIONS

[1]Grupo de Mecánica de Fluidos, Universidad Carlos III, Leganés, Madrid 28911, Spain
[2]Center for Turbulence Research, Stanford University, Stanford, California 94305, USA

[a]Author to whom correspondence should be addressed: chuete@ing.uc3m.es

ABSTRACT

The interaction between a weakly turbulent free stream and a hypersonic shock wave is investigated theoretically by using linear interaction analysis (LIA). The formulation is developed in the limit in which the thickness of the thermochemical nonequilibrium region downstream of the shock, where relaxation toward vibrational and chemical equilibrium occurs, is assumed to be much smaller than the characteristic size of the shock wrinkles caused by turbulence. Modified Rankine–Hugoniot jump conditions that account for dissociation and vibrational excitation are derived and employed in a Fourier analysis of a shock interacting with three-dimensional isotropic vortical disturbances. This provides the modal structure of the post-shock gas arising from the interaction, along with integral formulas for the amplification of enstrophy, concentration variance, turbulent kinetic energy (TKE), and turbulence intensity across the shock. In addition to confirming known endothermic effects of dissociation and vibrational excitation in decreasing the mean post-shock temperature and velocity, these LIA results indicate that the enstrophy, anisotropy, intensity, and TKE of the fluctuations are much more amplified through the shock than in the thermochemically frozen case. In addition, the turbulent Reynolds number is amplified across the shock at hypersonic Mach numbers in the presence of dissociation and vibrational excitation, as opposed to the attenuation observed in the thermochemically frozen case. These results suggest that turbulence may persist and get augmented across hypersonic shock waves despite the high post-shock temperatures.

Published under an exclusive license by AIP Publishing. https://doi.org/10.1063/5.0059948

I. INTRODUCTION

Strong shock waves participate in a number of problems in physics, including the dynamics of high-energy interstellar medium,[1–4] the explosions of giant stars,[5–8] the fusion of matter in inertial-confinement devices,[9–11] and the ignition of combustible mixtures by lasers.[12,13] In addition to those, an important contemporary problem of relevance for aeronautical and astronautical engineering is the aerothermodynamics of hypersonic flight.[14,15] In hypersonics, similarly to the aforementioned problems, the intense compression of the gas through the shock waves generated by the fuselage leads to high temperatures that can activate complex thermochemical phenomena.[16] In particular, at high Mach numbers of up to approximately 25 in the terrestrial atmosphere, corresponding to sub-ionizing, sub-orbital stagnation enthalpies of up to approximately 15–30 MJ/kg depending on altitude, vibrational excitation, and air dissociation are the dominant thermochemical phenomena typically observed in the gas downstream of shock waves around hypersonic flight systems.

Turbulence can also play an important role at the high Mach numbers mentioned above, particularly in low-altitude hypersonic flight because of the correspondingly larger Reynolds numbers of the airflow around the fuselage.[17–19] However, the way in which turbulence influences the thermomechanical loads and the thermochemistry around hypersonic flight systems remains largely unknown. To compound this problem, experiments in the area of hypersonic turbulence are curtailed by the exceedingly large flow powers required to move gases at sufficiently high Mach and Reynolds numbers in order to observe shock waves simultaneously with turbulence and thermochemistry. In addition, the airflow in most ground facilities is poisoned with weak free-stream turbulence that interacts with the shock waves enveloping the test article. The fluctuations in the post-shock gases induced by this interaction oftentimes lead to artificial transition to turbulence in hypersonic boundary layers in wind tunnel experiments.[20]

Most early work on the interaction of shock waves with turbulence has been limited to calorically perfect gases in boundary layers[21–30] and isotropic free streams.[31–35] Large-scale numerical simulations, including Direct Numerical Simulations (DNS),[36–50] Large Eddy Simulations (LES),[51–53] and Reynolds-Averaged Navier-Stokes

Simulations (RANS),[54,55] have been the pacing item for those investigations. Nonetheless, the rapid progress in large-scale numerical simulations during the last decades has not abated the fundamental role that theoretical analyses have played in understanding shock/turbulence interactions by providing closed-form solutions. In problems dealing with shock waves propagating in turbulent free streams, as in the problem treated in the present study, the most successful theoretical approach has been the linear interaction analysis (LIA) pioneered by Ribner.[56–58]

Under the assumption that turbulence is comprised of small linear fluctuations that can be separated using Kovaznay's decomposition into vortical, entropic, and acoustic modes,[59] LIA describes their two-way coupled interaction with the shock by using linearized Rankine–Hugoniot jump conditions coupled with the linearized Euler equations in the post-shock gas. The resulting formalism describes the wrinkles induced by turbulence on the shock and the corresponding Kovaznay's compressible turbulence modes radiated by the interaction toward the downstream gas.

Despite its simplicity and limitations, LIA has not only provided a valuable insight into the underlying physical processes of shock/turbulence interactions, but has also worked sufficiently well for predicting the amplification of the turbulent kinetic energy (TKE), that is, commonly used for bench-marking numerical simulations.[38–40] However, there exist known discrepancies between LIA and numerical simulations in the way that TKE is distributed among the diagonal components of the Reynolds stress tensor. For instance, LIA yields a smaller (larger) amplification of TKE associated with streamwise (transverse) velocity fluctuations relative to that observed in numerical simulations. These discrepancies are typically attributed to the fact that LIA treats the shock as a discontinuity, in that DNS results are observed to converge to those obtained by LIA when the ratio of the numerical shock thickness to the Kolmogorov length scale becomes sufficiently small.[41,43,45]

In this study, an extension that incorporates thermochemical effects of vibrational excitation and gas dissociation is made to the standard LIA previously applied to calorically perfect gases.[56–58,60] As in the standard LIA, the following conditions must be satisfied: (a) the root mean square (rms) of the velocity fluctuations u_ℓ needs to be much smaller than the speed of sound in both pre-shock and post-shock gases; (b) the amplitude of the streamwise displacement of the distorted shock from its mean position ξ_s needs to be much smaller than the upstream integral size of the turbulence ℓ; and (c) the eddy turnover time ℓ/u_ℓ needs to be much smaller than the molecular diffusion time ℓ^2/ν based on the kinematic viscosity ν, or equivalently, the turbulent Reynolds number $Re_\ell = u_\ell \ell/\nu$ needs to be large.

In addition to the conditions [(a)–(c)] stated above, the incorporation of thermochemical effects requires that the characteristic size of the shock wrinkles, which is of the same order as ℓ, needs to be much larger than the thickness ℓ_T of the thermochemical nonequilibrium region behind the shock, as depicted in Fig. 1. For instance, the value of ℓ_T behind a Mach-14 normal shock at a pressure equivalent to 45 km of altitude is approximately 1 cm (see page 503 in Ref. 61). In this thermochemical nonequilibrium region, the gas relaxes toward vibrational and chemical equilibrium in an intertwined manner, in that the vibrational energy of the molecules and their dissociation probability are coupled.[16,62] The value of ℓ_T is approximately given by the mean post-shock velocity multiplied by the sum of the characteristic time scales of dissociation and vibrational relaxation. Since both of
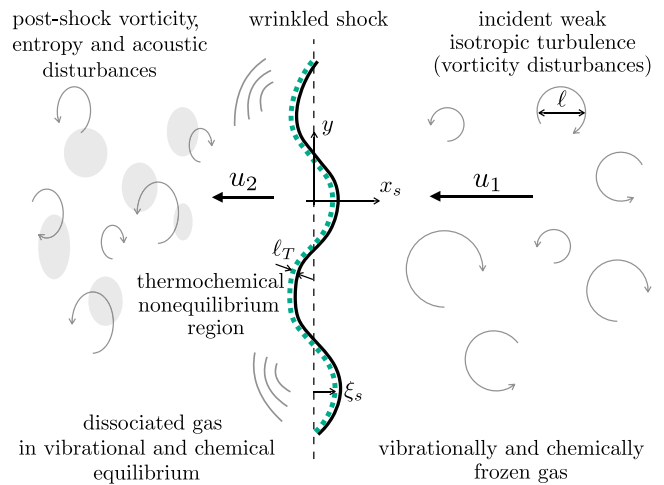

these characteristic time scales depend inversely on pressure and exponentially on the inverse of the temperature, the veracity of the approximation $\ell_T/\ell \ll 1$ in practical hypersonic systems is expected to improve as the flight Mach number increases and the altitude decreases.

The LIA results provided in this study yield integral formulas for the amplification of the enstrophy, composition variance, and TKE as a function of the post-shock Mach number, the density ratio, and the normalized inverse of the slope of the Hugoniot curve. The latter undergoes a change in sign at high Mach numbers due to the thermochemical effects. As a result, at Mach numbers larger than approximately 13 in the conditions tested here, a local decrement (increment) in post-shock pressure—due, for instance, to shock wrinkling—engenders an increment (decrement) in post-shock density. This peculiar structure of the Hugoniot curve at hypersonic Mach numbers is found to strongly amplify turbulence in the post-shock gas, where most of the TKE is observed to be contained in transverse velocity fluctuations of the vortical mode. For instance, the present LIA results in a maximum TKE amplification factor of approximately 2.9, whereas this value drops to 1.7 when the gas is assumed to be thermochemically frozen (i.e., diatomic calorically perfect).

The remainder of this paper is structured as follows. The Rankine–Hugoniot jump conditions across the shock are derived in Sec. II accounting for dissociation and vibrational excitation in the post-shock gas. A linearized formulation of the problem is presented in Sec. III for the interaction of a normal shock with monochromatic vorticity disturbances. A Fourier analysis is carried out in Sec. IV to address the interaction of a normal shock with weak isotropic turbulence composed of multiple and linearly superposed vorticity modes. Finally, conclusions are given in Sec. V.

II. RANKINE–HUGONIOT JUMP CONDITIONS WITH VIBRATIONAL EXCITATION AND GAS DISSOCIATION

We consider first the problem of an undisturbed, normal shock wave in a cold, inviscid, irrotational, single-component gas consisting

of symmetric diatomic molecules. The pre-shock density, pressure, temperature, specific internal energy, and flow velocity in the reference frame of the shock are denoted, respectively, as ρ_1, P_1, T_1, e_1, and u_1. The corresponding flow variables in the post-shock gas are denoted as ρ_2, P_2, T_2, e_2, and u_2.

A. Conservation equations across the shock

In the reference frame attached to the shock front, the conservation equations of mass, momentum, and enthalpy across the shock are

$$\rho_1 u_1 = \rho_2 u_2, \tag{1a}$$

$$P_1 + \rho_1 u_1^2 = P_2 + \rho_2 u_2^2, \tag{1b}$$

$$e_1 + P_1/\rho_1 + u_1^2/2 = e_2 + P_2/\rho_2 + u_2^2/2 + q_d, \tag{1c}$$

respectively. In this formulation, the symbol q_d denotes a positive quantity that represents the net change of specific chemical enthalpy caused by the gas dissociation reaction

$$\text{A}_2 \rightleftharpoons \text{A} + \text{A} \tag{2}$$

with A_2 being a generic molecular species and A its dissociated atomic counterpart. In particular, q_d can be expressed as

$$q_d = \alpha R_{g,\text{A}_2} \Theta_d, \tag{3}$$

where R_{g,A_2} is the gas constant based on the molecular weight of A_2, and Θ_d is the characteristic dissociation temperature. In addition, the variable α is the degree of dissociation defined as the ratio of the mass of dissociated A atoms to the total mass of the gas, or, equivalently, the mass fraction of A atoms.

Equations (1a)–(1c) are supplemented with the ideal-gas equations of state in the pre-shock gas

$$P_1/\rho_1 = R_{g,\text{A}_2} T_1 \tag{4}$$

and in the post-shock gas

$$P_2/\rho_2 = (1 + \alpha) R_{g,\text{A}_2} T_2. \tag{5}$$

In addition, the specific internal energy in the pre-shock gas e_1 is given by the translational and rotational components

$$e_1 = (5/2) R_{g,\text{A}_2} T_1, \tag{6}$$

whereas in the post-shock gas e_2 requires consideration of translational, rotational, and vibrational degrees of freedom along with mixing between molecular and atomic species, which gives

$$e_2 = R_{g,\text{A}_2} T_2 \left[3\alpha + (1 - \alpha) \left(\frac{5}{2} + \frac{\Theta_v/T_2}{e^{\Theta_v/T_2} - 1} \right) \right], \tag{7}$$

where Θ_v is the characteristic vibrational temperature. The first term inside the square brackets in (7), proportional to the dissociation degree α, corresponds to the translational contribution of the monatomic species. The second term, proportional to the factor $1 - \alpha$, includes the translational, rotational, and vibrational contributions of the molecular species, where it has been assumed that the rotational degrees of freedom are fully activated and the molecules vibrate as harmonic oscillators.

The formulation is closed with the chemical-equilibrium condition downstream of the shock, namely,[63]

$$\frac{\alpha^2}{1 - \alpha} = Gm\Theta_r \left(\frac{\pi m k_B}{\hbar^2} \right)^{3/2} \frac{\sqrt{T_2}}{\rho_2} e^{-\frac{\Theta_d}{T_2}} \left(1 - e^{-\frac{\Theta_v}{T_2}} \right), \tag{8}$$

where Θ_r is the characteristic rotational temperature, m is the atomic mass of A, k_B is the Boltzmann's constant, $\hbar$ is the reduced Planck's constant, and $G = (Q_{\text{el}}^a)^2/Q_{\text{el}}^{aa}$ is a ratio of electronic partition functions of A atoms (Q_{el}^a) and A_2 molecules (Q_{el}^{aa}). Upon neglecting the variations of the specific internal energy with temperature due to electronic excitation, the electronic partition functions in G can be approximated as the ground-state degeneracy factors. Typical values of Θ_r, Θ_v, Θ_d, G, and m are provided in Table I for a wide range of molecular gases.

B. Dimensionless formulation

A dimensionless formulation of the problem can be written by introducing the dimensionless parameters

$$B = \frac{Gm\Theta_r T_1^{1/2}}{\rho_1} \left(\frac{\pi m k_B}{\hbar^2} \right)^{3/2}, \quad \beta_d = \frac{\Theta_d}{T_1}, \quad \beta_v = \frac{\Theta_v}{T_1} \tag{9}$$

along with the pressure, temperature, and density jumps

$$\mathcal{P} = P_2/P_1, \quad \mathcal{T} = T_2/T_1, \quad \mathcal{R} = \rho_2/\rho_1 \tag{10}$$

across the shock. In the expressions below, the solution for a vibrationally and chemically frozen gas (i.e., a calorically perfect diatomic gas) is recovered by taking the limits $\beta_v \to \infty$ and $\beta_d \to \infty$ (or $\alpha \to 0$).

Using these definitions, the dimensionless Rayleigh line

$$\mathcal{P} = 1 + \frac{7}{5} \mathcal{M}_1^2 \left(1 - \frac{1}{\mathcal{R}} \right), \tag{11}$$

which relates $\mathcal{P}$ and $\mathcal{R}$, is obtained by combining the mass and momentum conservation equations (1a) and (1b). In (11), the symbol $\mathcal{M}_1$ denotes the pre-shock Mach number defined as

$$\mathcal{M}_1 = u_1/c_1, \tag{12}$$

where $c_1 = \sqrt{(7/5)R_{g,\text{A}_2} T_1}$ is the speed of sound of the pre-shock gas. Regardless of the value of $\mathcal{M}_1$, the Rayleigh line always emanates from the pre-shock state, $\mathcal{P} = 1$ and $\mathcal{R} = 1$, as a straight line with negative slope in the $\{\mathcal{R}^{-1}, \mathcal{P}\}$ plane.

In contrast, since the post-shock gas is calorically imperfect, its Mach number

$$\mathcal{M}_2 = \frac{u_2}{c_2} = \frac{\mathcal{M}_1}{\mathcal{R}} \frac{c_1}{c_2} \tag{13}$$

requires a more elaborate calculation of the speed of sound

TABLE I. Rotational (Θ_r), vibrational (Θ_v), and dissociation (Θ_d) characteristic temperatures, along with the factor G and the atomic mass m of relevant molecular gases.

	H_2	O_2	N_2	F_2	I_2	Cl_2
Θ_r (K)	87.53	2.08	2.87	1.27	0.0538	0.0346
Θ_v (K)	6338	2270	3390	1320	308	805
Θ_d (K)	51 973	59 500	113 000	18 633	17 897	28 770
G	$2^2/1$	$5^2/3$	$4^2/1$	$4^2/1$	$4^2/1$	$4^2/1$
m (kg) $\times 10^{26}$	0.167 35	2.6567	2.3259	3.1548	21.072	5.8871

$$c_2^2 = \frac{P_2}{\rho_2^2} \frac{\left.\frac{\partial P_2}{\partial T_2}\right|_{\rho_2}}{\left.\frac{\partial(e_2 + q_d)}{\partial T_2}\right|_{\rho_2}} - \frac{\left.\frac{\partial P_2}{\partial T_2}\right|_{\rho_2} \left.\frac{\partial(e_2 + q_d)}{\partial \rho_2}\right|_{T_2}}{\left.\frac{\partial(e_2 + q_d)}{\partial T_2}\right|_{\rho_2}} + \left.\frac{\partial P_2}{\partial \rho_2}\right|_{T_2}. \quad (14)$$

Upon substituting (5) and (7) into (14), the expression

$$\frac{c_2^2}{c_1^2} = \frac{5\mathcal{T}}{7} \left[1 + \alpha + \alpha_R + (1 + \alpha + \alpha_T) \right.$$
$$\left. \times \frac{2(1 + \alpha) - \alpha_R(1 - 2\bar{e}_{\text{vib}} + 2\beta_d/\mathcal{T})}{5 + \alpha + 2(1 - \alpha)\bar{e}_{\text{vib}}^2 e^{-\beta_v/\mathcal{T}} + \alpha_T(1 - 2\bar{e}_{\text{vib}} + 2\beta_d/\mathcal{T})} \right] \quad (15)$$

is obtained, where

$$\bar{e}_{\text{vib}} = \frac{\beta_v/\mathcal{T}}{e^{\beta_v/\mathcal{T}} - 1} \quad (16)$$

is the dimensionless component of the specific internal energy corresponding to vibrational excitation in equilibrium. In addition, the coefficients α_R and α_T in (15) are given by

$$\alpha_R = \mathcal{R}\left.\frac{\partial \alpha}{\partial \mathcal{R}}\right|_{\mathcal{T}} = -\frac{\alpha(1 - \alpha)}{2 - \alpha}, \quad (17)$$

$$\alpha_T = \mathcal{T}\left.\frac{\partial \alpha}{\partial \mathcal{T}}\right|_{\mathcal{R}} = -\alpha_R\left[\frac{1}{2} + \frac{\beta_d}{\mathcal{T}}\frac{1 - \left(1 + \frac{\beta_v}{\beta_d}\right)e^{-\beta_v/\mathcal{T}}}{1 - e^{-\beta_v/\mathcal{T}}}\right]. \quad (18)$$

Equation (15), along with definitions (16)–(18), determines the post-shock Mach number (13).

The equations of state (4) and (5) can be combined into a single equation as

$$\mathcal{P} = (1 + \alpha)\mathcal{R}\mathcal{T}. \quad (19)$$

Upon substituting (4)–(7) into the conservation equations (1a)–(1c) and using the normalizations (9) and (10), the relation

$$\mathcal{T} = \frac{6 - \mathcal{R}^{-1} - 2\alpha\beta_d - 2(1 - \alpha)\beta_v/(e^{\beta_v/\mathcal{T}} - 1)}{2(\alpha + 3) - \mathcal{R}(1 + \alpha)} \quad (20)$$

is obtained between α, $\mathcal{R}$, and $\mathcal{T}$. Finally, the problem is closed by rewriting the chemical-equilibrium condition (8) in dimensionless form using (9) and (10) as

$$\frac{\alpha^2}{1 - \alpha} = Be^{-\beta_d/\mathcal{T}}\frac{\sqrt{\mathcal{T}}}{\mathcal{R}}(1 - e^{-\beta_v/\mathcal{T}}), \quad (21)$$

which provides an additional relation between α, $\mathcal{R}$, and $\mathcal{T}$. In particular, given the dimensionless parameters β_v, β_d, and B, the combination of (19)–(21) provides the Hugoniot curve $\mathcal{P} = \mathcal{P}(\mathcal{R}^{-1})$, which in the present case is a laborious implicit function, that is, evaluated numerically and is shown in Fig. 2. As a result, given a pre-shock Mach number $\mathcal{M}_1$, the post-shock state is completely determined by the intersection of the Hugoniot curve and the Rayleigh line (11).

C. The turning point in the Hugoniot curve at hypersonic Mach numbers

It is worth discussing some peculiarities of the Hugoniot curve, that is, obtained by including dissociation and vibrational excitation
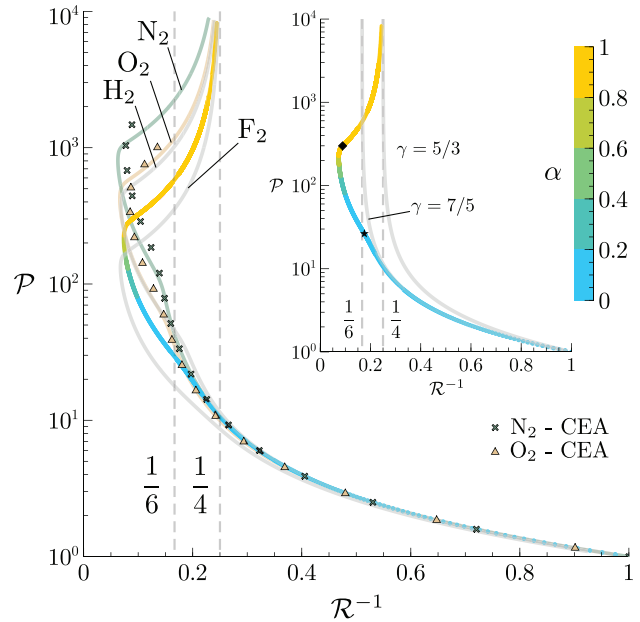

FIG. 2. Hugoniot curves for different molecular gases at pre-shock temperature $T_1 = 300$ K and pressure $P_1 = 1$ atm [gray lines: present formulation; symbols: numerical results obtained with NASA's Chemical Equilibrium with Applications (CEA) code[64] excluding ionization], along with the Hugoniot curve of a gas with $B = 10^6$, $\beta_v = 10$, and $\beta_d = 100$ (line colored by the degree of dissociation). The latter is compared in the inset with the Hugoniot curves of a calorically perfect monatomic gas (gray line corresponding to $\gamma = 5/3$) and a calorically perfect diatomic gas (gray line corresponding to $\gamma = 7/5$).

in the post-shock gas, since they are of some relevance for the shock/turbulence interaction problem studied in Secs. III and IV.

The main panel in Fig. 2 shows Hugoniot curves in light colors for H_2, O_2, N_2, and F_2 using the simple theory provided above particularized for the parameters B, β_v, and β_d listed in Table II. As shown in Fig. 2, the curves for O_2 and N_2 compare well with the more complex numerical calculations obtained with NASA's chemical equilibrium with applications (CEA) code.[64] The latter incorporates variations of the specific heat with temperature due to both vibrational and electronic excitation through the NASA polynomials.[65]

To narrow down the exposition, the main panel in Fig. 2 also shows a Hugoniot curve colored by the degree of dissociation and obtained using the representative values $B = 10^6$, $\beta_v = 10$, and $\beta_d = 100$. This is a particular choice of values that nonetheless approximately captures the order of magnitude of these parameters observed among the different gases listed in Table II (with exception

TABLE II. Dimensionless parameters B, β_v, and β_d for relevant molecular gases at pre-shock temperature $T_1 = 300$ K and pressure $P_1 = 1$ atm.

	H_2	O_2	N_2	F_2	I_2	Cl_2
$B \times 10^{-6}$	2.0668	6.472	14.0452	9.818	7.1796	0.6818
$\beta_v \times 10^{-1}$	2.1127	0.7567	1.13	0.44	0.1027	0.2683
$\beta_d \times 10^{-2}$	1.7324	1.9833	3.7667	0.6211	0.5966	0.959

of the much larger value of B observed for N_2, which translates into much higher dimensionless post-shock temperatures being required to attain significant dissociation of N_2).

The inset in Fig. 2 shows that the Hugoniot curve starts departing significantly from that of a calorically perfect diatomic gas [corresponding to an adiabatic coefficient $\gamma = 7/5$ and a maximum density ratio $\mathcal{R} = (\gamma + 1)/(\gamma - 1) = 6$] at a rather modest degree of dissociation $\alpha \sim 1\%$ attained at $\mathcal{M}_1 \sim 5$. Despite the smallness of this crossover value of α, large changes in chemical enthalpy occur because of the large bond-dissociation specific energy of most relevant species (e.g., approximately 15 MJ/kg for O_2). As a result, $\alpha \sim 1\%$ renders $\alpha \beta_d = O(1)$ in (20), which represents a balance between the heat absorbed by dissociation q_d and the pre-shock internal energy e_1 in the conservation equation (1c). As α is further increased, q_d becomes of the same order as e_2, and the departure from calorically perfect behavior becomes increasingly more pronounced.

As α becomes increasingly closer to unity, which requires the kinetic energy of the pre-shock gas to be increasingly larger than q_d (or equivalently, it requires the pre-shock Mach number $\mathcal{M}_1$ to be increasingly larger than $\sqrt{\beta_d}$), the slope of the Hugoniot curve undergoes a change in sign and turns inward toward larger specific volumes. For the parameters investigated in Fig. 2, the turning point occurs at $\alpha \simeq 0.7$, where $\mathcal{T} \simeq 9$ (corresponding to 2700 K when $T_1 = 300$ K), $\mathcal{M}_1 \simeq 13$, and $\mathcal{R} \simeq 12$, the latter being almost double (triple) the density ratio of a calorically perfect diatomic (mono-atomic) gas. There, the inverse of the slope of the Hugoniot curve normalized with the slope of the Rayleigh line

$$\Gamma = -\left(\frac{P_2 - P_1}{1/\rho_1 - 1/\rho_2}\right)\frac{\mathrm{d}(1/\rho_2)}{\mathrm{d}P_2} = \frac{7}{5}\frac{\mathcal{M}_1^2}{\mathcal{R}^2}\left(\frac{\partial \mathcal{P}}{\partial \mathcal{R}}\right)^{-1} \quad (22)$$

attains a zero value. The role of Γ in the description of the shock/turbulence interaction problem will be addressed in Secs. III and IV.

As shown in Fig. 3, the value of Γ becomes negative along the upper branch of the Hugoniot curve beyond the turning point $\Gamma = 0$. Along that branch, an increment (decrement) in post-shock pressure induces a decrement (increment) in post-shock density. For the parameters tested here, the value Γ in the upper branch of the Hugoniot curve is always larger than the critical values for the onset of (a) shock instabilities associated with multi-wave[66,67] and multi-valued[68] solutions, and (b) D'yakov–Kontorovich pseudo-instabilities associated with the spontaneous emission of sound.[8,69] Similar characteristics of the Hugoniot curve have been observed elsewhere for shocks subjected to endothermicity.[70–73]

D. Limit behavior in the post-shock gas

Typical distributions of the density ratio $\mathcal{R}$, the post-shock Mach number $\mathcal{M}_2$, and the pre-shock Mach number $\mathcal{M}_1$ are provided in Fig. 4 as a function of the temperature ratio $\mathcal{T}$. The curves also show the limit behavior for $\alpha \to 0$ and $\beta_v \to \infty$ (corresponding to a calorically perfect diatomic gas at low temperatures), and for $\alpha \to 1$ (corresponding to a fully dissociated gas at high temperatures). Some insight into these limits is provided below.

In Fig. 4(a), the low-temperature limit of the density ratio corresponds to the standard Rankine–Hugoniot jump condition for a calorically perfect diatomic gas
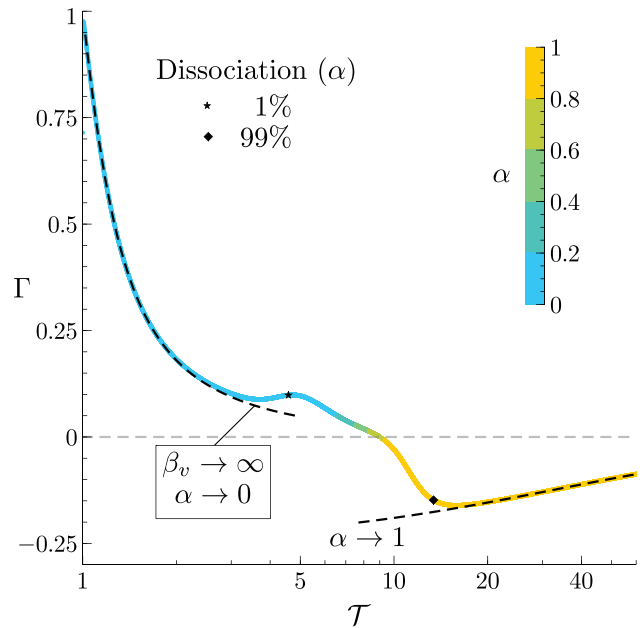

FIG. 3. Normalized inverse of the slope of the Hugoniot curve Γ as a function of the temperature jump across the shock $\mathcal{T}$ for $B = 10^6$, $\beta_v = 10$, and $\beta_d = 100$ (line colored by the degree of dissociation). Dashed lines represent asymptotic limits for a calorically perfect diatomic gas ($\beta_v \to \infty$ and $\alpha \to 0$), and for a highly dissociated gas ($\alpha \to 1$).

$$\mathcal{R} \sim 3\left(1 - \frac{1}{\mathcal{T}}\right)\left[1 + \sqrt{1 + \frac{\mathcal{T}}{9(\mathcal{T}-1)^2}}\right], \quad (23)$$

which can be derived by taking the limits $\alpha \to 0$ and $\beta_v \to \infty$ in (20). In this low-temperature limit, the normalized slope of the Hugoniot curve becomes $\Gamma \sim \mathcal{M}_1^{-2}$, as indicated in Fig. 3.

In the opposite limit, when the post-shock gas is hot and almost fully dissociated, $\alpha \to 1$, the density jump and the normalized slope of the Hugoniot curve become

$$\mathcal{R} \sim \frac{\beta_d + 4\mathcal{T} - 3 + \sqrt{(\beta_d + 4\mathcal{T} - 3)^2 + 2\mathcal{T}}}{2\mathcal{T}} \quad (24)$$

and

$$\Gamma \sim -\frac{7\mathcal{M}_1^2(\mathcal{R} - 4)^2}{5\mathcal{R}^2(8\beta_d - 23)}, \quad (25)$$

respectively, with $\beta_d > 23/8$ in the conditions tested here. At very high Mach numbers $\mathcal{M}_1 \gg \sqrt{\beta_d}$, when $\beta_d/\mathcal{T} \ll 1$, Eq. (24) simplifies to $\mathcal{R} \sim 4$ in the first approximation, whereas (25) yields very small and negative values of Γ. Remarkably, unlike $\mathcal{R}$, $\mathcal{M}_1$, and $\mathcal{M}_2$, the normalized inverse of the slope Γ is not bounded by its asymptotic limits at low and high Mach numbers. The relevance of this property for the problem of shock/turbulence interaction will be discussed in Secs. III and IV.

The results mentioned above for $\alpha \to 1$ indicate that the post-shock gas increasingly resembles a monatomic calorically perfect gas
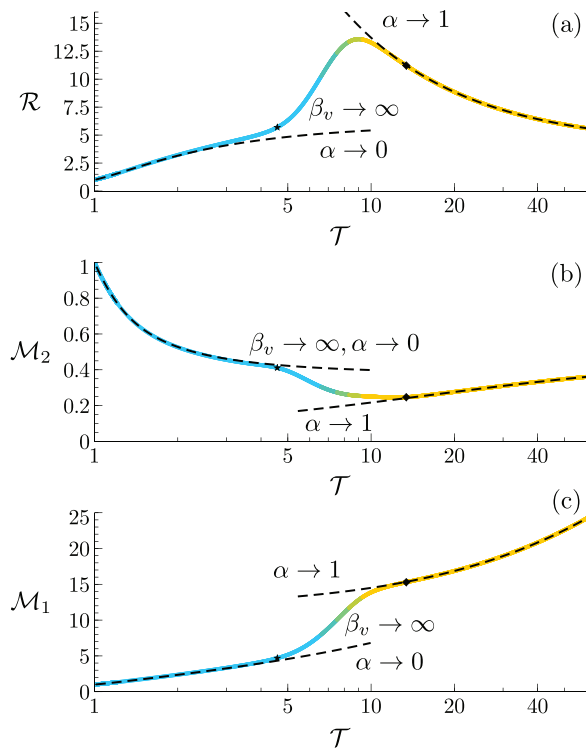
FIG. 4. Distributions of (a) density jump $\mathcal{R}$, (b) post-shock Mach number $\mathcal{M}_2$, and (c) pre-shock Mach number $\mathcal{M}_1$ as a function of the temperature jump $\mathcal{T}$ for $B = 10^6$, $\beta_v = 10$, and $\beta_d = 100$ (lines colored by the degree of dissociation; refer to Fig. 3 for a colorbar). Dashed lines represent asymptotic limits for a calorically perfect diatomic gas ($\beta_v \to \infty$ and $\alpha \to 0$), and for a highly dissociated gas ($\alpha \to 1$).

(corresponding to an adiabatic coefficient $\gamma = 5/3$ at infinite Mach numbers, an effect that can also be visualized in Fig. 2 as the Hugoniot curve asymptotes the abscissa $\mathcal{R}^{-1} \sim 1/4$. However, this limit is of little practical relevance because it would require such exceedingly high temperatures that additional effects like electronic excitation, radiation, and ionization would have to be included in the formulation, thereby invalidating these considerations.

III. THE INTERACTION OF A HYPERSONIC SHOCK WAVE WITH AN INCIDENT MONOCHROMATIC VORTICITY WAVE

For small-amplitude velocity fluctuations and vanishing turbulent Mach numbers, the free-stream turbulence in the pre-shock gas can be represented as a linear superposition of Kovaznay's three-dimensional vorticity modes, which are solutions of the incompressible Euler equations.[59,74] This section addresses the interaction of the shock with a single one of those vorticity modes.

A. Laboratory, shock, and post-shock reference frames

Three reference frames are used in the analysis. Whereas the spanwise and transverse axes of all the frames coincide, the streamwise axis differs depending on whether the frames are attached to the laboratory (x), the mean shock front (x_s), or the mean absolute post-shock gas motion (x_c).

In the laboratory reference frame, the streamwise coordinate is denoted by x and is attached to the bulk of the pre-shock gas, which is at rest on average. In contrast, in the shock reference frame, which corresponds to the one visualized in Fig. 1, the streamwise coordinate x_s moves at the mean shock velocity $\langle u_1 \rangle$ and is therefore defined by the relation $x_s = x - \langle u_1 \rangle t$ in terms of the time coordinate t. The integral formulation of the conservation equations across the shock can be readily written in the shock reference frame, as done in Sec. II. Whereas the incident vorticity wave remains stationary in space in the laboratory frame, it becomes a wave traveling at velocity $\langle u_1 \rangle$ toward the shock in the shock reference frame.

In the reference frame moving with the post-shock gas, the streamwise coordinate x_c moves with the post-shock mean absolute velocity $\langle u_1 \rangle - \langle u_2 \rangle$ and is therefore defined as $x_c = x - (\langle u_1 \rangle - \langle u_2 \rangle)t$. In this frame, the vorticity and entropy fluctuations in the post-shock gas are stationary in space, which facilitates the description of the problem, as shown below.

B. Orientation and form of the incident vorticity wave

Anticipating that the pre-shock turbulence is isotropic, there is no privileged direction of the wavenumber vector $\boldsymbol{k}$, and therefore, the amplitude of the vorticity modes depends exclusively on $k = |\boldsymbol{k}|$. Similarly, because of this isotropy, there is no preferred wavenumber-vector orientation relative to the shock surface. In principle, this would require the formulation of a three-dimensional problem to describe the interaction. However, a simple rotation of the reference frame can transform the problem into a two-dimensional one, as described below (see also Refs. 36, 60, and 75).

For an incident wavenumber vector arbitrary oriented in space at latitude and longitude angles θ and φ, respectively, the reference frames described in Sec. III A can be rotated counterclockwise around x by an angle equal to the longitudinal inclination of the incident wave ψ, as indicated in Fig. 5. In this way, the interaction problem becomes two-dimensional, in that all variations with respect to z are zero.

Using the aforementioned rotation, the wavenumber-vector components in the streamwise and transverse directions are

$$k_x = k\cos\theta, \quad k_y = k\sin\theta, \tag{26}$$

respectively, with $k_z = 0$ by construction. Similarly, in the laboratory reference frame, the vorticity vector of the incident wave in the pre-shock gas can be expressed as
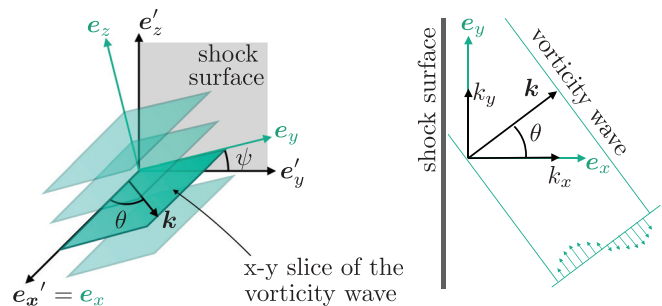

FIG. 5. Simplification of a three-dimensional problem of a shock interacting with an arbitrary-oriented vorticity wave to a two-dimensional problem by rotating the reference frame around the streamwise axis.

$$\boldsymbol{\omega_1} = (\delta\boldsymbol{\omega_1})e^{i(k_x x + k_y y)} \tag{27}$$

with

$$\delta\omega_{x,1} = -\varepsilon k \langle c_2 \rangle \sin\theta\cos\varphi, \quad \delta\omega_{y,1} = \varepsilon k \langle c_2 \rangle \cos\theta\cos\varphi,$$
$$\delta\omega_{z,1} = -\varepsilon k \langle c_2 \rangle \sin\varphi \tag{28}$$

being the vorticity amplitude in each direction. In this formulation, $\langle c_2 \rangle$ denotes the mean speed of sound in the post-shock gas, and ε is a dimensionless velocity fluctuation amplitude, which is small in the linear theory, $\varepsilon \ll 1$. The vorticity of the incident wave engenders a fluctuation velocity field in the pre-shock gas given by

$$\mathbf{v_1} = (\delta\mathbf{v_1})e^{i(k_x x + k_y y)} \tag{29}$$

whose amplitude is

$$\delta u_1 = \varepsilon \langle c_2 \rangle \sin\theta\sin\varphi, \quad \delta v_1 = -\varepsilon \langle c_2 \rangle \cos\theta\sin\varphi,$$
$$\delta w_1 = \varepsilon \langle c_2 \rangle \cos\varphi \tag{30}$$

in the x, y, and z directions, respectively. Specifically, the z-component of the fluctuation velocity vector is uniform along z. This component will not be carried any further in the analysis, since it is transmitted unaltered through the shock because of the conservation of tangential momentum. Note also that (27) and (29) are related by the definition of the vorticity $\boldsymbol{\omega_1} = \boldsymbol{k} \times \mathbf{v_1}$. Furthermore, the velocity field (29)–(30) is one that satisfies the incompressibility relation $\boldsymbol{k} \cdot \mathbf{v_1} = 0$. Finally, implicit in the definitions given above is that the incident vorticity wave is inviscid, or equivalently, that the pre-shock Reynolds number of the fluctuation, $2\pi|\mathbf{v_1}|/(k\nu_1)$, is infinitely large.

To illustrate the analysis, a particular form of the pre-shock vorticity fluctuation corresponding to the inviscid Taylor–Green vortex

$$\omega_{z,1}(x,y) = \varepsilon_u \langle c_2 \rangle \left(\frac{k^2}{k_y}\right) \cos(k_x x)\sin(k_y y) \tag{31}$$

is employed in the numerical results highlighted below, with $\omega_{x,1} = \omega_{y,1} = 0$. The corresponding streamwise and transverse components of the velocity fluctuations in the pre-shock gas are given by

$$u_1(x,y) = \varepsilon_u \langle c_2 \rangle \cos(k_x x)\cos(k_y y), \tag{32a}$$

$$v_1(x,y) = \varepsilon_u \langle c_2 \rangle \left(\frac{k_x}{k_y}\right) \sin(k_x x)\sin(k_y y), \tag{32b}$$

respectively. In this formulation, ε_u is the amplitude of the pre-shock streamwise velocity fluctuations

$$\varepsilon_u = \varepsilon \sin\theta\sin\varphi \tag{33}$$

with $\epsilon_u \ll 1$ in the linear theory.

C. Linearized formulation of the interaction problem

In this linear theory, the vorticity and the streamwise and transverse velocity components in the post-shock gas reference frame are expanded to first order in ε_u as

$$\omega = \varepsilon_u k_y \langle c_2^2 \rangle \bar{\omega}, \quad u = \varepsilon_u \langle c_2 \rangle \bar{u}, \quad v = \varepsilon_u \langle c_2 \rangle \bar{v}, \tag{34}$$

respectively, with $\bar{\omega}$, $\bar{u}$, and $\bar{v}$ being the corresponding dimensionless fluctuations. The post-shock pressure and density can be similarly expressed as

$$P = \langle P_2 \rangle + \varepsilon_u \langle \rho_2 \rangle \langle c_2 \rangle^2 \bar{p}, \quad \rho = \langle \rho_2 \rangle (1 + \varepsilon_u \bar{\rho}) \tag{35}$$

with $\bar{p}$ and $\bar{\rho}$ being the dimensionless fluctuations of pressure and density, respectively. The brackets indicate time-averaged quantities, which are given by the solution obtained in Sec. II. In this way, all fluctuations are defined to have a zero time average.

Assuming that the Reynolds number of the post-shock fluctuations is infinitely large, the expansions (34) and (35) can be employed in writing the linearized Euler conservation equations of mass, streamwise momentum, transverse momentum, and energy as

$$\frac{\partial\bar{\rho}}{\partial\tau} + \frac{\partial\bar{u}}{\partial\bar{x}_c} + \frac{\partial\bar{v}}{\partial\bar{y}} = 0, \tag{36a}$$

$$\frac{\partial\bar{u}}{\partial\tau} + \frac{\partial\bar{p}}{\partial\bar{x}_c} = 0, \tag{36b}$$

$$\frac{\partial\bar{v}}{\partial\tau} + \frac{\partial\bar{p}}{\partial\bar{y}} = 0, \tag{36c}$$

$$\frac{\partial\bar{p}}{\partial\tau} = \frac{\partial\bar{\rho}}{\partial\tau}, \tag{36d}$$

in the reference frame moving with the post-shock gas. In this notation, the space and time coordinates have been non-dimensionalized as

$$\bar{x}_c = k_y x_c, \quad \bar{y} = k_y y, \quad \tau = k_y \langle c_2 \rangle t. \tag{37}$$

The linearized Euler equations (36) can be combined into a single, two-dimensional periodically symmetric wave equation

$$\frac{\partial^2\bar{p}}{\partial\tau^2} = \frac{\partial^2\bar{p}}{\partial\bar{x}_c^2} + \frac{\partial^2\bar{p}}{\partial\bar{y}^2} \tag{38}$$

for the post-shock pressure fluctuations. Equation (38) is integrated for $\tau \geq 0$ within the spatiotemporal domain bounded by the leading reflected sonic wave traveling upstream, $\bar{x}_c = -\tau$, and the shock front moving downstream $\bar{x}_c = \mathcal{M}_2\tau$, with $\mathcal{M}_2 = \langle u_2 \rangle/\langle c_2 \rangle$.

In the integration of (38), the boundary condition far downstream of the shock is provided by the isolated-shock assumption, whereby the effect of the acoustic waves reaching the shock front from behind is neglected. The boundary condition at the shock front is obtained from the linearized Rankine–Hugoniot jump conditions assuming that (a) the thickness of the thermochemical non-equilibrium region ℓ_T is much smaller than the inverse of the transverse wavenumber k_y^{-1}; and (b) the displacement of the shock $\xi_s = \xi_s(y,t)$ from its mean, flat shape (see Fig. 1) is much smaller than k_y^{-1}. In these limits, at any transverse coordinate $\bar{y}$, the Rayleigh–Hugoniot jump conditions can be applied at the mean shock front location $\bar{x}_c = \mathcal{M}_2\tau$ and can be linearized about the mean thermochemical-equilibrium post-shock gas state $\mathcal{P}$, $\mathcal{R}$, $\mathcal{T}$, $\mathcal{M}_2$, and α calculated in Sec. II, thereby yielding

$$\frac{\partial\bar{\xi}_s}{\partial\tau} = \frac{\mathcal{R}(1-\Gamma)}{2\mathcal{M}_2(\mathcal{R}-1)}\bar{p}_s - \bar{u}_1, \tag{39a}$$

$$\bar{u}_s = \frac{1+\Gamma}{2\mathcal{M}_2}\bar{p}_s + \bar{u}_1, \tag{39b}$$

$$\bar{v}_s = \bar{v}_1 - \mathcal{M}_2(\mathcal{R}-1)\frac{\partial\bar{\xi}_s}{\partial\bar{y}}, \tag{39c}$$

$$\bar{\rho}_s = \frac{\Gamma}{\mathcal{M}_2^2}\bar{p}_s. \tag{39d}$$

In (39), $\bar{\bar{\xi}}_s = k_y \xi_s / \varepsilon_u$ is the dimensionless shock displacement, whereas $\bar{p}_s$, $\bar{\rho}_s$, $\bar{u}_s$, and $\bar{v}_s$ are, respectively, the dimensionless fluctuations of pressure, density, streamwise velocity, and transverse velocity immediately downstream of the shock front, where thermochemical equilibrium is reached in the limit $k_y \ell_T \ll 1$. In these relations, $\bar{u}_1 = u_1/(\varepsilon_u \langle c_2 \rangle)$ and $\bar{v}_1 = v_1/(\varepsilon_u \langle c_2 \rangle)$ are the normalized components of the pre-shock velocity field (29) engendered by the incident wave described in Sec. III B. Note that, at the turning point of the Hugoniot curve ($\Gamma = 0$), the compression of the gas exerted by the shock is isochoric in the near field and therefore leads to vanishing density fluctuations immediately downstream of the shock, as prescribed by the linearized jump condition (39d).

The flow is periodic in the transverse direction $\bar{y}$. As a result, the terms involving partial derivatives with respect to $\bar{y}$ in (36a), (36c), (38), and (39c) can be easily calculated from the transverse functional form of the post-shock flow variables given the incident vorticity wave (31). In particular, it can be shown that the fluctuations $\bar{p}$, $\bar{u}$, and $\bar{\bar{\xi}}_s$ are proportional to $\cos(\bar{y})$, whereas $\bar{v}$ is proportional to $\sin(\bar{y})$. These prefactors are henceforth omitted in the analysis, but should be brought back when reconstructing the full solution from the dimensionless fluctuations.

The initial conditions required to solve (38) assume that the shock is initially flat, $\bar{\bar{\xi}}_s = \bar{v}_s = 0$ at $\tau = 0$. Correspondingly, the initial values of the fluctuations of pressure and streamwise velocity immediately downstream of the shock must satisfy the relation $\bar{u}_s + \bar{p}_s = 0$ at $\tau = 0$, as prescribed by the first acoustic wave traveling upstream $x_c = -\tau$. This gives a pressure fluctuation $\bar{p}_s = -2\mathcal{M}_2/(1 + \Gamma + 2\mathcal{M}_2)$ immediately downstream of the shock front at $\tau = 0$.

The linearized problem (38), along with its boundary and initial conditions provided above, describe the fluctuations in the post-shock gas in the LIA framework. Remarkably, this problem can be integrated using the mean post-shock flow obtained from the analytical formulation provided in Sec. II, as done in the remainder of this paper, or by considering a mean post-shock flow obtained numerically with more sophisticated thermochemistry. For instance, instead of the formulation presented in Sec. II, a one-dimensional chemical equilibrium code like CEA (see Fig. 2 and Sec. II C) could be used to calculate numerically the mean post-shock conditions incorporating (a) different models for the variations of the specific heats such as the NASA polynomials,[65] which include both vibrational and electronic excitation, and (b) additional chemical effects such as ionization. This can be understood by noticing that (38), along with its boundary and initial conditions, depend only on the following dimensionless parameters: the mean density jump $\mathcal{R}$, the mean post-shock Mach number $\mathcal{M}_2$, and the inverse of the slope of the Hugoniot curve Γ, all of which can be computed numerically solving a one-dimensional shock wave subject to arbitrary thermochemistry.

D. Far-field and long-time asymptotic analysis

At long times $t \gg (k_y \langle c_2 \rangle)^{-1}$, the solution to the wave equation (38), subject to the boundary conditions described in Sec. III C, yields the pressure fluctuations

$$\bar{p}_s = \begin{cases} \Pi_{l1} \cos(\omega\tau) + \Pi_{l2} \sin(\omega\tau) & \text{if } \zeta \leq 1, \\ \Pi_s \cos(\omega\tau) & \text{if } \zeta \geq 1 \end{cases} \tag{40}$$

behind the shock. In this formulation, $\omega = \zeta\sqrt{1 - \mathcal{M}_2^2}$ is the dimensionless frequency, where ζ is a frequency parameter defined as

$$\zeta = \frac{\mathcal{M}_2\mathcal{R}}{\sqrt{1 - \mathcal{M}_2^2}}\left(\frac{k_x}{k_y}\right) \tag{41}$$

with $k_x/k_y = 1/|\tan\theta|$. Cases with $\zeta \leq 1$ correspond to sufficiently small streamwise wavenumbers, $k_x \leq k_y\left(\sqrt{1 - \mathcal{M}_2^2}\right)/(\mathcal{M}_2\mathcal{R})$, whereas the opposite (sufficiently large streamwise wavenumbers) holds for $\zeta \leq 1$. The corresponding amplitudes of the pressure wave (40) are

$$\Pi_{l1} = -\frac{(1 - \mathcal{R}^{-1})(\sigma_b\zeta^2 - \sigma_c)}{\zeta^2(1 - \zeta^2) + (\sigma_b\zeta^2 - \sigma_c)^2}\left(\zeta^2 - \frac{\mathcal{R}\mathcal{M}_2^2}{1 - \mathcal{M}_2^2}\right), \tag{42a}$$

$$\Pi_{l2} = \frac{(1 - \mathcal{R}^{-1})\zeta\sqrt{1 - \zeta^2}}{\zeta^2(1 - \zeta^2) + (\sigma_b\zeta^2 - \sigma_c)^2}\left(\zeta^2 - \frac{\mathcal{R}\mathcal{M}_2^2}{1 - \mathcal{M}_2^2}\right), \tag{42b}$$

$$\Pi_s = -\frac{(1 - \mathcal{R}^{-1})}{\zeta\sqrt{\zeta^2 - 1} + \sigma_b\zeta^2 - \sigma_c}\left(\zeta^2 - \frac{\mathcal{R}\mathcal{M}_2^2}{1 - \mathcal{M}_2^2}\right), \tag{42c}$$

where σ_b and σ_c are auxiliary factors defined as

$$\sigma_b = \frac{1 + \Gamma}{2\mathcal{M}_2}, \quad \sigma_c = \frac{\mathcal{R}\mathcal{M}_2}{1 - \mathcal{M}_2^2}\left(\frac{1 - \Gamma}{2}\right). \tag{43}$$

To describe the far-field post-shock gas, it is convenient to split the fluctuations of velocity, pressure, and density into their acoustic (a), vortical (r), and entropic (e) components as

$$\bar{u}(\bar{x}_c, \tau) = \bar{u}_a(\bar{x}_c, \tau) + \bar{u}_r(\bar{x}_c), \tag{44a}$$

$$\bar{v}(\bar{x}_c, \tau) = \bar{v}_a(\bar{x}_c, \tau) + \bar{v}_r(\bar{x}_c), \tag{44b}$$

$$\bar{p}(\bar{x}_c, \tau) = \bar{p}_a(\bar{x}_c, \tau), \tag{44c}$$

$$\bar{\rho}(\bar{x}_c, \tau) = \bar{\rho}_a(\bar{x}_c, \tau) + \bar{\rho}_e(\bar{x}_c). \tag{44d}$$

The acoustic pressure wave emerging from (38) is of the form $\bar{p}_a \sim e^{\pm i(\omega_a\tau - \kappa_a\bar{x} - \bar{y})}$, where ω_a and κ_a are the dimensionless acoustic frequency and longitudinal wavenumber reduced with $c_2 k_y$ and k_y, respectively, which are related as

$$\omega_a^2 = \kappa_a^2 + 1. \tag{45}$$

In the shock reference frame $\bar{x} = \mathcal{M}_2\tau$, the oscillation frequency at shock front, ω, is related to the post-shock Mach number as $\omega = \omega_a - \mathcal{M}_2\kappa_a$. Upon substituting this relation into (45), the expressions

$$\kappa_a = \frac{\mathcal{M}_2\omega \pm \sqrt{\omega^2 - 1 + \mathcal{M}_2^2}}{1 - \mathcal{M}_2^2}, \tag{46a}$$

$$\omega_a = \frac{\omega \pm \mathcal{M}_2\sqrt{\omega^2 - 1 + \mathcal{M}_2^2}}{1 - \mathcal{M}_2^2} \tag{46b}$$

are obtained. In (46), the solution corresponding to the positive sign in front of the square root must be excluded since it represents nonphysical acoustic waves whose amplitude increases exponentially with distance downstream of the shock when $\omega < (1 - \mathcal{M}_2^2)^{1/2}$.

Different forms of the solution arise depending on the value of the dimensionless frequency ω. At frequencies $\omega < (1 - \mathcal{M}_2^2)^{1/2}$, or equivalently $\zeta < 1$, the amplitude of the acoustic pressure decreases exponentially with distance downstream of the shock. On the other hand, for $\omega > (1 - \mathcal{M}_2^2)^{1/2}$, or $\zeta > 1$, the acoustic pressure becomes a constant-amplitude wave

$$\bar{p}(\bar{x}_c, \tau) = \Pi_s \cos(\omega_a \tau - \kappa_a \bar{x}_c), \tag{47}$$

which corresponds to a downstream-traveling sound wave for $\kappa_a < 0$ (or $\omega < 1$), and to an upstream-traveling sound wave for $\kappa_a > 0$ ($\omega > 1$), both cases being referenced to the post-shock gas reference frame. In this case, the acoustic modes of the density, temperature, and velocities are

$$\bar{\rho}_a(\bar{x}_c, \tau) = \Pi_s \cos(\omega_a \tau - \kappa_a \bar{x}_c), \tag{48a}$$
$$\bar{T}_a(\bar{x}_c, \tau) = \Theta_a \cos(\omega_a \tau - \kappa_a \bar{x}_c), \tag{48b}$$
$$\bar{u}_a(\bar{x}_c, \tau) = \mathcal{U}_a \cos(\omega_a \tau - \kappa_a \bar{x}_c), \tag{48c}$$
$$\bar{v}_a(\bar{x}_c, \tau) = \mathcal{V}_a \sin(\omega_a \tau - \kappa_a \bar{x}_c), \tag{48d}$$

respectively, where $\bar{T} = (T - \langle T_2 \rangle)/(\varepsilon_u \langle T_2 \rangle)$ is the dimensionless post-shock temperature fluctuation.

The amplitudes of the acoustic modes of the streamwise and transverse velocity fluctuations in (48) are proportional to the amplitude of the acoustic pressure, $\mathcal{U}_a/\Pi_s = \kappa_a/\omega_a$ and $\mathcal{V}_a/\Pi_s = 1/\omega_a$, as prescribed by second and third equations in (36). Similarly, the amplitude of the acoustic mode of the post-shock temperature fluctuations can be expressed relative to Π_s as

$$\Theta_a/\Pi_s = \frac{2(1+\alpha) - \alpha_R(1 - 2\bar{e}_{\text{vib}} + 2\beta_d/\mathcal{T})}{5 + \alpha + 2(1-\alpha)\bar{e}_{\text{vib}}^2 e^{-\beta_v/\mathcal{T}} + \alpha_T(1 - 2\bar{e}_{\text{vib}} + 2\beta_d/\mathcal{T})} \tag{49}$$

with α_R, α_T, and $\bar{e}_{\text{vib}}$ being defined in (17) and (18), and (16), respectively. Note that (49) simplifies to $\Theta_a/\Pi_s \sim \gamma - 1$ in both the calorically perfect diatomic gas limit ($\alpha \to 0$ and $\beta_v \to \infty$, for which $\gamma \to 7/5$) and in the fully dissociated gas limit ($\alpha \to 1$, for which $\gamma \to 5/3$).

The entropic mode of the density fluctuations is determined by the linearized Rankine–Hugoniot jump condition (39d) after subtracting the acoustic mode

$$\bar{\rho}_e(\bar{x}_c) = \frac{\Gamma}{\mathcal{M}_2^2} \bar{p}_s(\tau = \bar{x}_c/\mathcal{M}_2) - \bar{\rho}_a(\bar{x}_c, \tau = \bar{x}_c/\mathcal{M}_2) \tag{50}$$

to give

$$\bar{\rho}_e(\bar{x}_c \gg 1) = \begin{cases} \Delta_{l1} \cos(\kappa_e \bar{x}_c) + \Delta_{l2} \sin(\kappa_e \bar{x}_c) & \text{if } \zeta \leq 1, \\ \Delta_s \cos(\kappa_e \bar{x}_c) & \text{if } \zeta \geq 1 \end{cases} \tag{51}$$

in the asymptotic far field. In (51), $\kappa_e = \mathcal{R} k_x/k_y$ is a dimensionless wavenumber, and $\Delta_j = (\Gamma \mathcal{M}_2^{-2} - 1)\Pi_j$ is a fluctuation amplitude that depends on ζ through the pressure amplitudes Π_{l1}, Π_{l2}, and Π_s defined in (42). Since the pre-shock gas contains only vortical velocity fluctuations, all entropic modes are generated at the shock. The entropic density fluctuations $\bar{\rho}_e$ are related to the entropic temperature fluctuations

$$\bar{T}_e(\bar{x}_c \gg 1) = -\frac{1 + \alpha + \alpha_R}{1 + \alpha + \alpha_T} \bar{\rho}_e(\bar{x}_c), \tag{52}$$

and both $\bar{\rho}_e$ and $\bar{T}_e$ induce entropic fluctuations in the degree of dissociation, as shown in (8). As a result, the thermochemical equilibrium state in the post-shock gas fluctuates depending on the local shock curvature. Specifically, there exist fluctuations of the concentrations of the chemical species A and A_2 in the post-shock gas that are in phase with the entropic modes of density and temperature fluctuations. The normalized fluctuation of the degree of dissociation is

$$\bar{\alpha}(\bar{x}_c \gg 1) = \frac{\alpha - \langle \alpha \rangle}{\varepsilon_u} = \alpha_R \bar{\rho}_e(\bar{x}_c) + \alpha_T \bar{T}_e(\bar{x}_c)$$
$$= \frac{(\alpha_R - \alpha_T)(1 + \alpha)}{1 + \alpha + \alpha_T} \bar{\rho}_e(\bar{x}_c). \tag{53}$$

In a similar manner, the vorticity fluctuations $\bar{\omega}$ defined in (34) can be expressed in terms of ζ as

$$\bar{\omega}(\bar{x}_c \gg 1) = \begin{cases} \Omega_l \cos(\kappa_r \bar{x}_c + \phi_r) & \text{if } \zeta \leq 1, \\ \Omega_s \cos(\kappa_r \bar{x}_c) & \text{if } \zeta \geq 1, \end{cases} \tag{54}$$

where, as found in the entropic perturbation field, the dimensionless rotational wavenumber is simply given by the compressed upstream wavenumber ratio $\kappa_r = \kappa_e = \mathcal{R} k_x/k_y$. The amplitudes are

$$\Omega_l = \sqrt{(\Omega_1 + \Omega_2 \Pi_{l1})^2 + (\Omega_2 \Pi_{l2})^2}, \tag{55a}$$
$$\Omega_s = \Omega_1 + \Omega_2 \Pi_s, \tag{55b}$$

where $\Omega_1 = \mathcal{R}(1 + k_x^2/k_y^2)$ quantifies the amplification of the pre-shock vorticity as a direct result of the shock compression, and $\Omega_2 = (\mathcal{R} - 1)(1 - \Gamma)/(2\mathcal{M}_2)$ measures the vorticity production by the discontinuity front rippling. The corresponding phase for $\zeta < 1$ is given by $\tan \phi_r = \Omega_2 \Pi_{l2}/(\Omega_1 + \Omega_2 \Pi_{l1})$, which is different to that associated with entropic fluctuations $\tan \phi_e = \Pi_{l2}/\Pi_{l1}$.

Figure 6 shows the value of $|\Omega|^2$ as a function of the shock strength $\mathcal{M}_1$ for six arbitrary values of the frequency parameter ζ.
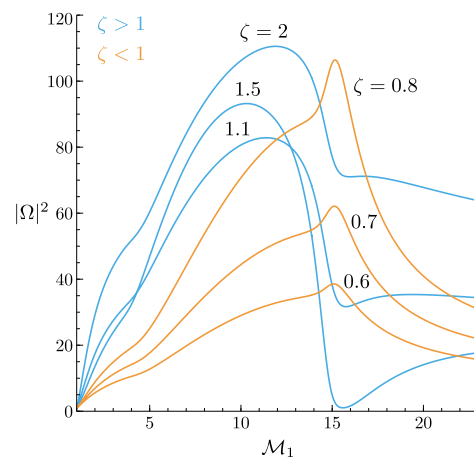

FIG. 6. Square of the vorticity amplitude $|\Omega|^2$ as a function of the pre-shock Mach number $\mathcal{M}_1$ for $B = 10^6$, $\beta_v = 10$, $\beta_d = 100$ and six different values of the frequency parameter: $\zeta = 0.6, 0.7, 0.8, 1.1, 1.5,$ and 2.

Three of them pertain to the long-wavelength regime $\zeta < 1$ ($\Omega = \Omega_l$) and the other three to the short-wavelength regime $\zeta > 1$ ($\Omega = \Omega_s$). It is found that the shape of the curve qualitatively changes depending on the wavelength regime. For instance, when compared to interactions with frequency $\zeta < 1$, cases for $\zeta > 1$ render curves with wider peaks and whose location corresponds to lower Mach numbers.

The streamwise and transverse components of the vortical mode of the velocity read

$$\bar{u}_r(\bar{x}_c \gg 1) = \mathcal{U}_r \cos(\kappa_r \bar{x}_c + \phi_r), \tag{56a}$$

$$\bar{v}_r(\bar{x}_c \gg 1) = \mathcal{V}_r \sin(\kappa_r \bar{x}_c + \phi_r), \tag{56b}$$

where the phase angle is $\phi_r = 0$ for $\zeta > 1$. The amplitudes are proportional to the vorticity fluctuations as

$$\mathcal{U}_r = \frac{1}{1 + \kappa_r^2}\Omega = \frac{\mathcal{M}_2^2}{\mathcal{M}_2^2 + (1 - \mathcal{M}_2^2)\zeta^2}\Omega, \tag{57a}$$

$$\mathcal{V}_r = \frac{\kappa_r}{1 + \kappa_r^2}\Omega = \frac{\zeta \mathcal{M}_2 \sqrt{1 - \mathcal{M}_2^2}}{\mathcal{M}_2^2 + (1 - \mathcal{M}_2^2)\zeta^2}\Omega, \tag{57b}$$

where Ω depends on frequency, as shown in (55) and Fig. 6.

IV. THE INTERACTION OF A HYPERSONIC SHOCK WAVE WITH WEAK ISOTROPIC TURBULENCE

The weak isotropic turbulence in the pre-shock gas can be represented by a linear superposition of incident vorticity waves whose amplitudes ε vary with the wavenumber in accord with an isotropic energy spectrum $E(k) = \varepsilon^2(k)$. The root mean square (rms) of the velocity and vorticity fluctuations in the pre-shock gas can be calculated by invoking the isotropy assumption, which states that the probability the incident wave has of having orientation angles ranging from θ to $\theta + d\theta$, and from φ to $\varphi + d\varphi$, is proportional to the solid angle $\sin\theta d\theta d\varphi/(4\pi)$. This assumption provides the expressions

$$\frac{\langle u_1'^2 \rangle}{\varepsilon^2 \langle c_2 \rangle^2} = \frac{1}{3}, \quad \frac{\langle v_1'^2 \rangle}{\varepsilon^2 \langle c_2 \rangle^2} = \frac{1}{6}, \quad \frac{\langle w_1'^2 \rangle}{\varepsilon^2 \langle c_2 \rangle^2} = \frac{1}{2} \tag{58}$$

for the pre-shock rms velocity fluctuations, and

$$\frac{\langle \omega_{x,1}'^2 \rangle}{\varepsilon^2 k^2 \langle c_2 \rangle^2} = \frac{1}{3}, \quad \frac{\langle \omega_{y,1}'^2 \rangle}{\varepsilon^2 k^2 \langle c_2 \rangle^2} = \frac{1}{6}, \quad \frac{\langle \omega_{z,1}'^2 \rangle}{\varepsilon^2 k^2 \langle c_2 \rangle^2} = \frac{1}{2} \tag{59}$$

for the pre-shock vorticity fluctuations. In this section, a linear analysis is performed to calculate the variations of the rms of the velocity and vorticity fluctuations across the shock.

A. Amplifications of turbulent kinetic energy, turbulence intensity, and turbulent Reynolds number across the shock

The analysis begins by expressing pre-shock components of the velocity fluctuation modulus as

$$|u_2'| = c_2 \varepsilon |\bar{u}_a + \bar{u}_r| \sin\theta \sin\varphi, \tag{60a}$$

$$|v_2'| = c_2 \varepsilon |\bar{v}_a + \bar{v}_r| \sin\theta \sin\varphi, \tag{60b}$$

$$|w_2'| = |w_1'|, \tag{60c}$$

where the acoustic and vortical modes of the dimensionless velocity fluctuations in the far field are given in (48) and (56). The relations between the modes of the streamwise and transverse velocity fluctuations are provided by the irrotationality condition $\bar{v}_a = \kappa_a \bar{u}_a$ for the acoustic mode, and by the solenoidal condition $k_y \bar{v}_r = \mathcal{R} k_x \bar{u}_r$ for the vortical mode.

The TKE amplification factor across the shock wave is defined as

$$
\begin{aligned}
K &= \frac{\langle u_2'^2 \rangle + \langle v_2'^2 \rangle + \langle w_2'^2 \rangle}{\langle u_1'^2 \rangle + \langle v_1'^2 \rangle + \langle w_1'^2 \rangle} = \frac{\langle u_2'^2 \rangle + \langle v_2'^2 \rangle}{\varepsilon^2 \langle c_2 \rangle^2} + \frac{1}{2} \\
&= \frac{1}{2}\left[\int_0^{\pi/2} (\bar{u}^2 + \bar{v}^2)\sin^3\theta d\theta + 1\right],
\end{aligned} \tag{61}
$$

where the use of (58) has been made. Furthermore, K can also be decomposed linearly into acoustic and vortical modes as $K = K^a + K^r$, with

$$
\begin{aligned}
K^a &= \frac{1}{3}\int_1^\infty (\mathcal{U}_a^2 + \mathcal{V}_a^2)\mathrm{P}(\zeta)d\zeta = \frac{1}{3}\int_1^\infty \Pi_s^2 \mathrm{P}(\zeta)d\zeta, \\
K^r &= \frac{1}{2} + \frac{1}{3}\int_0^\infty (\mathcal{U}_r^2 + \mathcal{V}_r^2)\mathrm{P}(\zeta)d\zeta.
\end{aligned} \tag{62}
$$

The entropic mode does not contain any kinetic energy, since entropy fluctuations are decoupled from velocity fluctuations in the inviscid linear limit.

In Eq. (62), $\mathrm{P}(\zeta)$ is a probability-density distribution given by

$$\mathrm{P}(\zeta) = \frac{3}{2}\frac{\mathcal{M}_2^4 \mathcal{R}^4 \sqrt{1 - \mathcal{M}_2^2}}{\left[\mathcal{M}_2^2 \mathcal{R}^2 + \zeta^2(1 - \mathcal{M}_2^2)\right]^{5/2}}, \tag{63}$$

which satisfies the normalization $\int_0^\infty \mathrm{P}(\zeta)d\zeta = 1$. In addition, the velocity amplitudes $\mathcal{U}_a$, $\mathcal{U}_r$, $\mathcal{V}_a$, and $\mathcal{V}_r$ are obtained using the long-time far-field asymptotic expressions (48) and (57). The lower integration limit of K^a is $\zeta = 1$ since the acoustic mode decays exponentially with distance downstream of the shock in the long-wave regime $\zeta < 1$. However, the integral $1/3 \int_0^1 (\Pi_{l1}^2 + \Pi_{l1}^2)\mathrm{P}(\zeta)d\zeta$ needs to be added to K^a when evaluating the solution in the near field $\bar{x}_s - \bar{x}_c \ll 1$.

Figure 7 shows the TKE amplification factor K, given by the sum of the acoustic and vortical contributions in (62), as a function of the pre-shock Mach number $\mathcal{M}_1$. Similarly to the results observed in Sec. II, the onset of vibrational excitation at $\mathcal{M}_1 \sim 3$ begins to produce small departures of K from the thermochemically frozen result corresponding to a diatomic calorically perfect gas. These departures are exacerbated as the degree of dissociation increases and become significant even at small values of α of order 1% at $\mathcal{M}_1 \sim 5$, where K significantly departs from the curve predicted in the thermochemically frozen limit corresponding to a diatomic calorically perfect gas. The latter was shown to plateau at $K = 1.78$ for $\mathcal{M}_1 \gg 1$ in early work,[37,60] whereas the present study indicates that such plateau does not exist when thermochemical effects at hypersonic Mach numbers are accounted for.

The resulting curve of K in Fig. 7 is non-monotonic and contains two peaks in the hypersonic range of Mach numbers. This behavior cannot be guessed by a simple inspection of the post-shock density and Mach number shown in Fig. 4. Instead, the non-monotonicity of K is related to the strong dependence of the enstrophy amplification on the wavenumber. Specifically, the vortical mode of the velocity fluctuation, which is shown below to be the most energetic, is proportional to the post-shock vorticity amplitude Ω given in (55), which peaks at
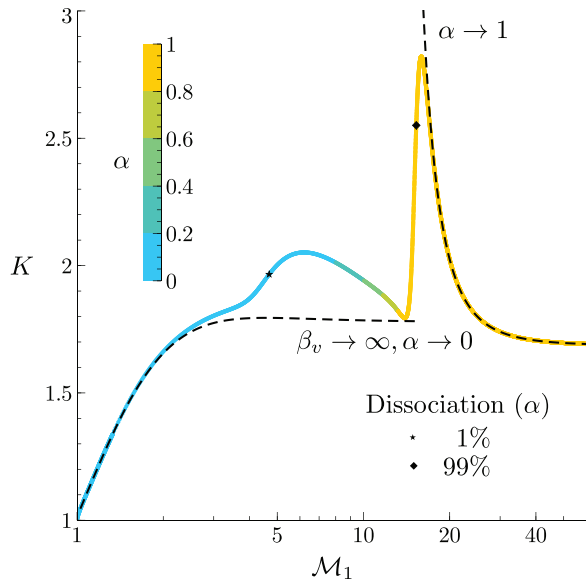
FIG. 7. TKE amplification factor K as a function of the pre-shock Mach number $\mathcal{M}_1$ for $B = 10^6$, $\beta_v = 10$, and $\beta_d = 100$ (line colored by the degree of dissociation). Dashed lines correspond to limit behavior of K calculated using the asymptotic expressions (23) and (24) for small and high Mach numbers, respectively.

different pre-shock Mach numbers depending on the frequency parameter ζ, as shown in Fig. 6.

The first peak of K reaches a value of 2.1 and occurs at $\mathcal{M}_1 \sim 6$, where $\alpha \sim 5\%$. In contrast, the second peak at $K \sim 2.9$ nearly doubles the value predicted in the thermochemically frozen limit, and occurs at a much higher Mach number $\mathcal{M}_1 \sim 19$ where dissociation is almost complete. At very large Mach numbers $\mathcal{M}_1 > 40$, in the fully dissociated regime, K asymptotes to the value $K \sim 1.69$ predicted for monatomic calorically perfect gases. However, as discussed in Sec. II D, this limit has to be interpreted with caution because additional thermochemical effects not included here, such as ionization and electronic excitation, play an important role at those extreme Mach numbers.

Most of the TKE produced across the shock belongs to transverse velocity fluctuations of the vortical mode. To see this, we consider the decomposition of the TKE amplification factor into longitudinal (K_L) and transverse (K_T) components as

$$K = \frac{1}{3}(K_L + 2K_T) \qquad (64)$$

with

$$K_L = \underbrace{\int_1^\infty \mathcal{U}_a^2 \mathrm{P}(\zeta)\mathrm{d}\zeta}_{\substack{K_L^a \\ \text{kinetic energy of the} \\ \text{longitudinal acoustic mode}}} + \underbrace{\int_0^\infty \mathcal{U}_r^2 \mathrm{P}(\zeta)\mathrm{d}\zeta}_{\substack{K_L^r \\ \text{kinetic energy of the} \\ \text{longitudinal vortical mode}}} , \qquad (65a)$$

$$K_T = \underbrace{\frac{1}{2}\int_1^\infty \mathcal{V}_a^2 \mathrm{P}(\zeta)\mathrm{d}\zeta}_{\substack{K_T^a \\ \text{kinetic energy of the} \\ \text{transverse acoustic mode}}} + \underbrace{\frac{3}{4} + \frac{1}{2}\int_0^\infty \mathcal{V}_r^2 \mathrm{P}(\zeta)\mathrm{d}\zeta}_{\substack{K_T^r \\ \text{kinetic energy of the} \\ \text{transverse vortical mode}}} . \qquad (65b)$$

The contribution of the acoustic mode to K_L and K_T yields negligible TKE over the entire range of Mach numbers, as shown in Fig. 8(a). In contrast, the contribution of the vortical mode is significant. Whereas the longitudinal TKE of the vortical mode K_L^r dominates over the transverse one K_T^r at supersonic Mach numbers, it plunges below K_T^r at hypersonic Mach numbers around the turning point of the Hugoniot curve. The value of K_T^r peaks at $\mathcal{M}_1 \sim 19$ with $K_T^r \sim 3.8$, as observed in Fig. 8(b). This peak is responsible for the peak in K observed Fig. 7 at the same Mach number, thereby indicating that most the TKE there is stored in vortical gas motion in the transverse direction.

The mechanism whereby high-temperature thermochemistry augments the TKE across the shock in this LIA framework is explained by the linearized Rankine–Hugoniot jump condition (39c) and is schematically shown in Fig. 9. In particular, the conservation of the tangential velocity across the wrinkled shock requires

$$\begin{aligned} v_t &= \langle u_1 \rangle \cos\vartheta + v_1' \sin\vartheta \\ &= \langle u_2 \rangle \cos\vartheta + v_2' \sin\vartheta, \end{aligned} \qquad (66)$$

where $\vartheta = \pi/2 + \arctan(\partial \xi_s / \partial y)$ is a local shock incidence angle whose departures from $\pi/2$ are of order ϵ_u, since $k_y \xi_s = O(\epsilon_u)$ in this linear theory. The streamwise velocity fluctuations u_1' and u_2' have been neglected in writing (66), since their multiplication by $\cos\beta$ is smaller by a factor of order ϵ_u relative to the other terms. Equation (66) yields the transverse post-shock velocity fluctuation

$$v_2' = v_1' - (\langle u_1 \rangle - \langle u_2 \rangle) \frac{\partial \xi_s}{\partial y}, \qquad (67)$$

which represents the dimensional counterpart of the linearized Rankine–Hugoniot jump condition (39c). In Eq. (67), $\partial \xi_s / \partial y < 0$ in both configurations sketched in Fig. 9. Note that (67) holds
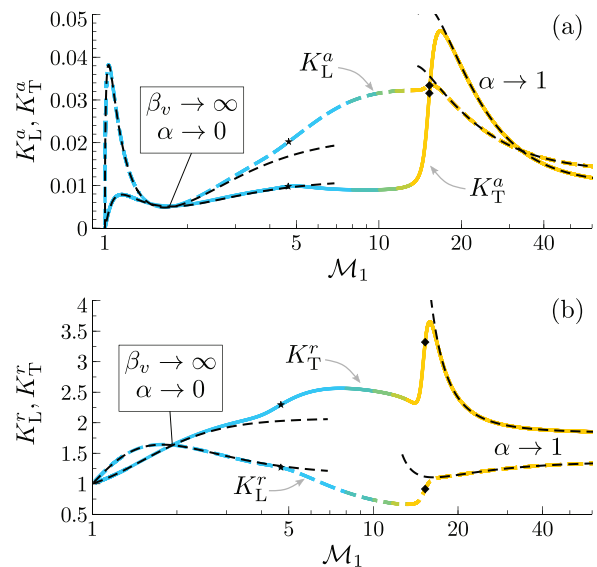

FIG. 8. (a) Acoustic and (b) vortical modes of the streamwise (K_L) and transverse (K_T) components of the TKE amplification factor as a function of the pre-shock Mach number $\mathcal{M}_1$ for $B = 10^6$, $\beta_v = 10$, and $\beta_d = 100$ (lines colored by the degree of dissociation; refer to Fig. 7 for a colorbar). Dashed lines correspond to limit behavior of K_L and K_T calculated using the asymptotic expressions (23) and (24) for small and high Mach numbers, respectively.
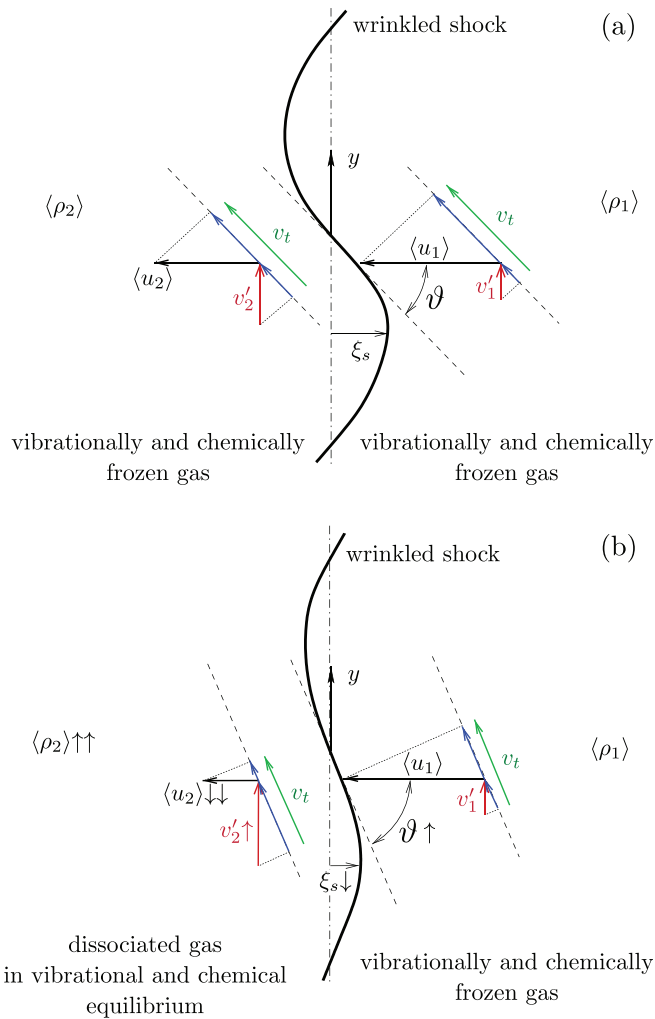
FIG. 9. Schematics of the mechanism of TKE amplification for (a) thermochemically frozen (i.e., diatomic calorically perfect) post-shock gas, and (b) thermochemically equilibrated post-shock gas, both panels simulating the same pre-shock conditions. The flow is from right to left. The magnitude of the shock displacement and velocity perturbations has been exaggerated for illustration purposes.

independently of whether the gas is thermochemically frozen or equilibrated. However, the thermochemistry influences (67) by flattening the shock front (i.e., by decreasing $\partial \xi_s / \partial y$) while strongly decreasing the mean post-shock velocity $\langle u_2 \rangle = \langle u_1 \rangle / \mathcal{R}$, with the latter effect prevailing over the former. As a result, v_2' and its associated kinetic energy K_T are larger relative to those observed in a diatomic calorically perfect gas.

The TKE amplification, along with the aforementioned decrease in the mean post-shock velocity $\langle u_2 \rangle$ caused by the thermochemical effects, also leads to a strong amplification of the turbulence intensity across the shock. Specifically, the ratio of post- to pre-shock turbulence intensities

$$\frac{\mathcal{I}_2}{\mathcal{I}_1} = \frac{u_{\ell,2}/\langle u_2 \rangle}{u_{\ell,1}/\langle u_1 \rangle} = K^{1/2}\mathcal{R} \tag{68}$$

is found to peak at the turning point of the Hugoniot curve ($\alpha \simeq 0.7$, $\mathcal{T} \simeq 9$, $\mathcal{M}_1 \simeq 13$, and $\mathcal{R} \simeq 12$) with a value $\mathcal{I}_2/\mathcal{I}_1 \simeq 19$, as shown in Fig. 10(a). This is in contrast to the maximum value $\mathcal{I}_2/\mathcal{I}_1 \simeq 8$ predicted by the theory of calorically perfect gases.

Although the theory presented above is formulated in the inviscid limit, the ratio of post- to pre-shock turbulent Reynolds numbers

$$\frac{Re_{\ell,2}}{Re_{\ell,1}} = \frac{u_{\ell,2}\ell_2/\nu_2}{u_{\ell,1}\ell_1/\nu_1} = \frac{K^{1/2}}{\mathcal{T}^{0.7}}\sqrt{\frac{2\mathcal{R}^2 + 1}{3}} \tag{69}$$

is a finite quantity that can be calculated. In the last term of (69), the use has been made of the fact that the only wavenumber, that is, distorted through the shock is the longitudinal one, which changes from k_x in the pre-shock fluctuations to $k_x\mathcal{R}$ in the post-shock ones. In addition, the molecular viscosity is assumed to vary with temperature raised to the power of 0.7.

Remarkably, the vortical post-shock fluctuations downstream of the hypersonic shock are not only much more intense than those upstream, but they also have a higher turbulent Reynolds number $Re_{\ell,2} > Re_{\ell,1}$, as shown in Fig. 10(b). Similarly to the turbulence intensities, the maximum ratio of turbulent Reynolds numbers across the shock is reached at the turning point of the Hugoniot curve ($\alpha \simeq 0.7$, $\mathcal{T} \simeq 9$, $\mathcal{M}_1 \simeq 13$, and $\mathcal{R} \simeq 12$) with a value of $Re_{\ell,2}/Re_{\ell,1} \simeq 5$. In contrast, the theory of calorically perfect gases predicts an attenuation of the turbulent Reynolds number at those conditions. When thermochemical effects are accounted for, the amplification of the turbulent Reynolds number lasts until $\mathcal{M}_1 \simeq 20$, beyond which the increase in post-shock temperature and the decrease in post-shock density make $Re_{\ell,2}/Re_{\ell,1}$ to plummet below unity.

In summary, the increase in transverse velocity fluctuations of the vortical mode across the shock is responsible for the TKE amplification
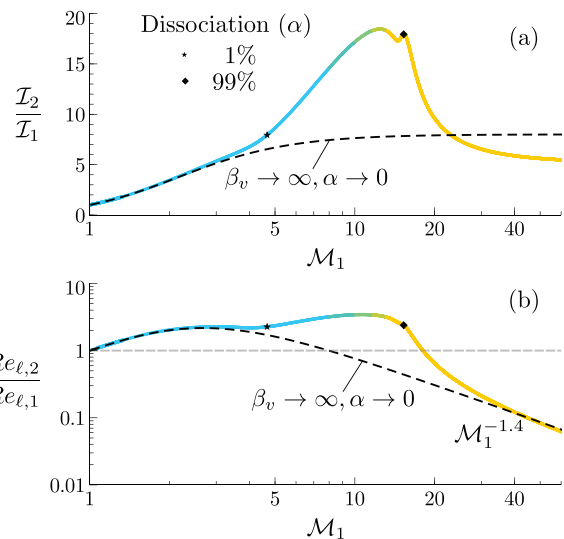

FIG. 10. Amplification of (a) turbulence intensity and (b) turbulent Reynolds number across the shock as a function of the pre-shock Mach number $\mathcal{M}_1$ for $B = 10^6$, $\beta_v = 10$, and $\beta_d = 100$ (lines colored by the degree of dissociation; refer to Fig. 7 for a colorbar). The dashed lines correspond to the values of $\mathcal{I}_2/\mathcal{I}_1$ and $Re_{\ell,2}/Re_{\ell,1}$ calculated assuming that the post-shock gas is thermochemically frozen (i.e., diatomic calorically perfect).

in this linear theory. In addition, the results indicate that the TKE is more amplified when dissociation and vibrational excitation are accounted for at high Mach numbers. In the conditions tested here, the post-shock fluctuations resulting at hypersonic Mach numbers can be—at most—19 times more intense and can have—at most—a five times larger turbulent Reynolds number than the pre-shock fluctuations.

B. Amplifications of anisotropy, enstrophy, and variances of density and degree of dissociation across the shock

The weak isotropic turbulence in the pre-shock gas becomes anisotropic as it traverses the shock wave. An anisotropy factor that quantifies this change can be defined as[60]

$$\Psi = \frac{\langle \overline{v^2} \rangle + \langle \overline{w^2} \rangle - 2\langle \overline{u^2} \rangle}{\langle \overline{v^2} \rangle + \langle \overline{w^2} \rangle + 2\langle \overline{u^2} \rangle} = 1 - \frac{2K_L}{K_L + K_T} \tag{70}$$

with $-1 \leq \Psi \leq 1$. The cases $\Psi = -1$ and 1 represent anisotropic turbulent flows dominated by longitudinal and transverse velocity fluctuations, respectively. In contrast, $\Psi = 0$ corresponds to an isotropic turbulent flow, $K_T = K_L = K$. Figure 11 shows that dissociation and vibrational excitation dissociation lead to larger anisotropy factors in the post-shock gas compared to the thermochemically frozen (diatomic calorically perfect) case in the relevant range of hypersonic Mach numbers up to the fully dissociated gas limit.

The vortical motion downstream of the shock is quantified by the enstrophy amplification factor

$$W = \frac{\langle \omega_{x,2}'^2 \rangle + \langle \omega_{y,2}'^2 \rangle + \langle \omega_{z,2}'^2 \rangle}{\langle \omega_{x,1}'^2 \rangle + \langle \omega_{y,1}'^2 \rangle + \langle \omega_{z,1}'^2 \rangle} = \frac{1}{3} + \frac{2}{3} W_\perp, \tag{71}$$
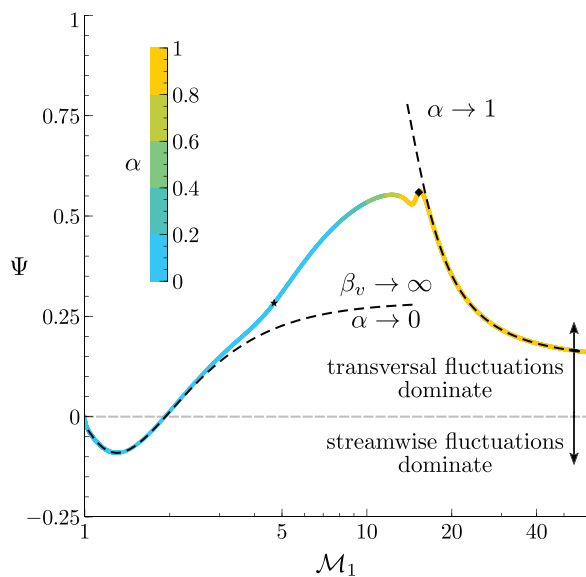
where the use of (59) and of the invariance of the normal vorticity across the shock has been made. In (71), $W_\perp$ is the enstrophy amplification factor in the transverse direction

$$W_\perp = \frac{1}{3} + \frac{2}{3} \frac{\langle \omega_{y,2}'^2 \rangle + \langle \omega_{z,2}'^2 \rangle}{\langle \omega_{y,1}'^2 \rangle + \langle \omega_{z,1}'^2 \rangle} = \frac{\mathcal{R} + 3W_z}{4} \tag{72}$$

with

$$W_z = \frac{\langle \omega_{z,2}'^2 \rangle}{\langle \omega_{z,1}'^2 \rangle} = \int_0^\infty \Omega^2 \frac{\mathcal{R}^2 \mathcal{M}_2^2 \, \mathrm{P}(\zeta)}{\mathcal{R}^2 \mathcal{M}_2^2 + (1 - \mathcal{M}_2^2)\zeta^2} \, \mathrm{d}\zeta \tag{73}$$

being the amplification factor of the rms of the $z-$component of the vorticity. Equation (73) includes the asymptotic amplitudes defined in (55) and the relation

$$\sin^2\theta(\zeta)\mathrm{P}(\zeta) = \frac{3}{2} \frac{\mathcal{M}_2^6 \mathcal{R}^6 \sqrt{1 - \mathcal{M}_2^2}}{\left[\mathcal{M}_2^2 \mathcal{R}^2 + \zeta^2 (1 - \mathcal{M}_2^2) \right]^{7/2}}. \tag{74}$$

The enstrophy amplification factor W is provided in Fig. 12 as a function of the pre-shock Mach number. Similarly to Fig. 7 for K, the curve of W displays two maxima, but the differences with respect to the thermochemically frozen case are much larger for W. The first peak of W is dominated by the increase in short-wavelength vorticity, as shown in Fig. 6, and it represents an amplification of nearly four times the enstrophy predicted by the theory of calorically perfect gases.

Whereas the pre-shock density is uniform because of the vortical character of the incident modes, the density in the post-shock gas fluctuates due to both acoustic and entropic modes generated by the shock wrinkles. To investigate these fluctuations, we consider the normalized density variance
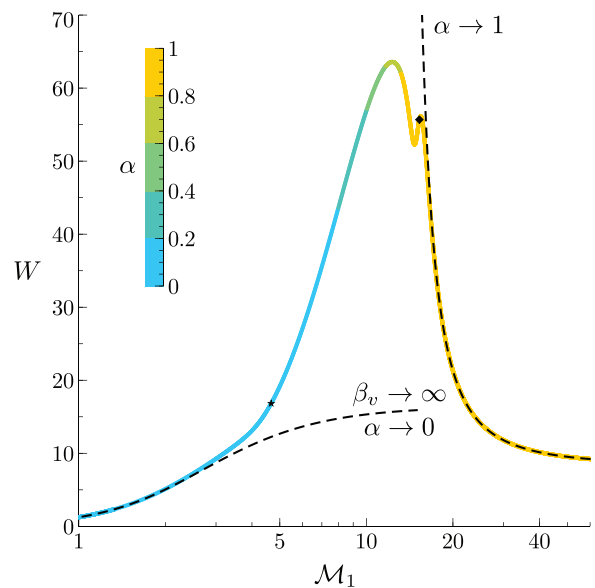

FIG. 11. Anisotropy factor Ψ as a function of the pre-shock Mach number $\mathcal{M}_1$ for $B = 10^6$, $\beta_v = 10$, and $\beta_d = 100$ (line colored by the degree of dissociation). Dashed lines correspond to limit behavior of Ψ calculated using the asymptotic expressions (23) and (24) for small and high Mach numbers, respectively.

FIG. 12. Enstrophy W as a function of the pre-shock Mach number $\mathcal{M}_1$ for $B = 10^6$, $\beta_v = 10$, and $\beta_d = 100$ (line colored by the degree of dissociation). Dashed lines correspond to limit behavior of W calculated using the asymptotic expressions (23) and (24) for small and high Mach numbers, respectively.

$$\frac{\langle \rho_2'^2 \rangle}{\langle \rho_2^2 \rangle} = (G^a + G^e) \int_0^\infty E(k)k^2 \mathrm{d}k, \tag{75}$$

which depends on the integral of the energy spectrum E over the entire wavenumber space. The prefactors G^a and G^e represent density-variance components induced by acoustic and entropic modes, respectively, and are given by

$$G^a = K^a, \tag{76a}$$

$$G^e = \left(\Gamma \mathcal{M}_2^{-2} - 1\right)^2 \int_0^1 \left(\Pi_{l1}^2 + \Pi_{l2}^2\right) \mathrm{P}(\zeta)\mathrm{d}\zeta$$
$$+ \left(\Gamma \mathcal{M}_2^{-2} - 1\right)^2 \int_1^\infty \Pi_s^2 \mathrm{P}(\zeta)\mathrm{d}\zeta, \tag{76b}$$

where the use of (51) has been made. Figure 13(a) shows that, while the vortical fluctuations across the shock are increased by dissociation, the density variance induced by the entropic mode is small for $\mathcal{M}_1 \lesssim 10$ but increases sharply thereafter up to $\mathcal{M}_1 \sim 19$, where it achieves a maximum value. As observed by comparing Figs. 8(b) and 13(a), the acoustic prefactor G^a is found to be negligible compared to the entropic one G^e.

Whereas the Rankine–Hugoniot jump condition (39d) evaluated at the turning point of the Hugoniot curve $\Gamma = 0$ indicates that the density fluctuations immediately downstream of the shock are zero, the entropic prefactor in Fig. 13(a) at $\mathcal{M}_1 \simeq 13$ (where Γ vanishes) leads to a non-zero density variance. The two results can be reconciled by noticing that the formulation in (76) and the approximation $G^e \gg G^a$ are applicable only to the far-field downstream of the shock. In contrast, the acoustic mode needs to be retained near the shock. Specifically, the post-shock density fluctuations in the

FIG. 13. Entropic prefactors of (a) the post-shock density variance and (b) the post-shock degree of dissociation as a function of the pre-shock Mach number $\mathcal{M}_1$ for $B = 10^6$, $\beta_v = 10$, and $\beta_d = 100$ (lines colored by the degree of dissociation; refer to Fig. 12 for a colorbar). Dashed lines correspond to limit behavior of G^e calculated using the asymptotic expressions (23) and (24) for small and high Mach numbers, respectively.

near field vanish as $\Gamma \to 0$ because of a destructive interference between the acoustic and entropic modes. In contrast, the entropic mode dominates in the far field and leads to non-zero post-shock density fluctuations.

The entropic component of the density variance engenders a variance of the degree of dissociation given by

$$\langle \alpha'^2 \rangle = A^e \int_0^\infty E(k)k^2 \mathrm{d}k, \tag{77}$$

where

$$A^e = \frac{(\alpha_R - \alpha_T)^2(1+\alpha)^2}{(1+\alpha+\alpha_T)^2} G^e \tag{78}$$

is the corresponding prefactor. Figure 13(b) shows that A^e attains a maximum value at $\mathcal{M}_1 \sim 15$, and becomes negligible both in the absence of dissociation and when dissociation is complete.

V. CONCLUSIONS

The interaction between a hypersonic shock wave and weak isotropic turbulence has been addressed in this work using LIA. Contrary to previous studies of shock/turbulence interactions focused on calorically perfect gases, the results provided here account for endothermic thermochemical effects of vibrational excitation and gas dissociation enabled by the high post-shock temperatures. Important approximations used in this theory are that the thickness of the thermochemical non-equilibrium region trailing the shock front is small compared to the characteristic size of the shock wrinkles, and that all fluctuations in the flow are small relative to the mean.

The results presented here indicate that the thermochemical effects act markedly on the solution in a number of important ways with respect to the results predicted by the theory of calorically perfect gases:

(a) Significant departures from calorically perfect-gas behavior can be observed in the solution even at modest degrees of dissociation of 1%, corresponding to Mach 5 and therefore to the beginning of the hypersonic range. This is because the associated bond-dissociation energies of typical molecules are large. As a result, the chemical enthalpy invested in dissociation in the post-shock gas can easily surpass the pre-shock thermal energy and become of the same order as the pre-shock kinetic energy.

(b) A turning point in the Hugoniot curve is observed at approximately Mach 13 and 70% degree of dissociation that leads to a significant increase of the mean post-shock density of approximately 12 times its pre-shock value, which represents nearly twice the maximum density jump predicted by the theory of calorically perfect gases.

(c) The aerothermodynamic behavior of the post-shock gas changes fundamentally around the turning point in the Hugoniot curve. As the Mach number increases above 13, positive fluctuations of streamwise velocity engender positive pressure fluctuations in the post-shock gas that are accompanied by negative density fluctuations. In this way, the local post-shock density and pressure are anticorrelated, although the shock remains stable to corrugations in all operating conditions tested here.
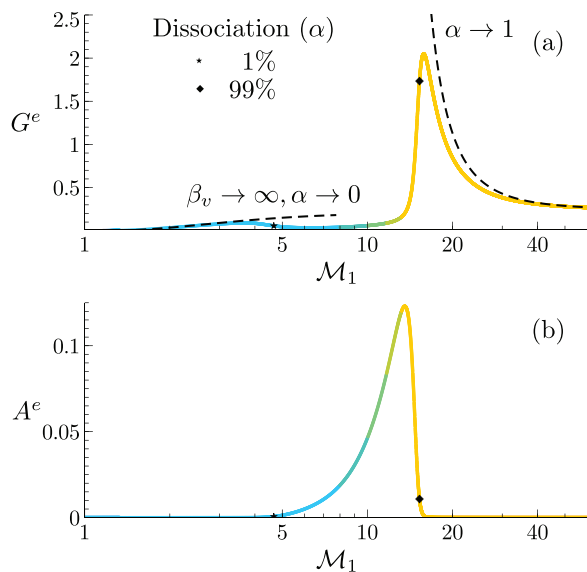
(d)   The amplification of TKE is larger than that observed in calorically perfect gases. Whereas the streamwise velocity fluctuations across the shock are decreased, the transverse ones are greatly increased (i.e., much more than in a diatomic calorically perfect gas). This phenomenon can be explained in the linear theory by using the conservation of tangential momentum, which elicits larger transverse velocity fluctuations as a result of the increase in post-shock density that occurs due to dissociation and vibrational excitation. This effect also leads to a much more significant increase of anisotropy and enstrophy across the shock than that observed in a diatomic calorically perfect gas.

(e)   Most of the amplified content of TKE is stored in vortical velocity fluctuation modes in the post-shock gas. The trend of the TKE amplification factor with the pre-shock Mach number is non-monotonic and involves two maximum values, one equal to 2.1 at Mach 6 (corresponding to a degree of dissociation of 5%), and a second one equal to 2.9 at Mach 19 (corresponding to a degree of dissociation larger than 99%).

(f)   The turbulence intensity and turbulent Reynolds number increase across the shock and reach maximum amplification factors of 19 and 5, respectively, both occurring at the turning point of the Hugoniot curve (Mach 13 and degree of dissociation of 70%). The maximum amplification factor of the turbulence intensity is more than twice the one attainable in a diatomic calorically perfect gas. The amplification of the turbulent Reynolds number observed here is in contrast with the attenuation predicted by the theory of calorically perfect gases at hypersonic Mach numbers.

(g)   The density variance in the post-shock gas is almost exclusively generated by entropic modes radiated by the shock wrinkles and nearly doubles the value predicted for calorically perfect gases. Similarly, the shock front generates entropic fluctuations of the concentration of atomic species that might be relevant for applications in supersonic combustion if the post-shock gas is going to be employed to oxidize the fuel.[14,76]

The LIA predictions for the overall TKE amplification factor in calorically perfect gases have been previously found to be in fair agreement with numerical simulations[36,38,39,49] and experiments.[33] However, the way LIA predicts the amplified TKE to be partitioned in the streamwise and transverse directions has not been as successful. In particular, computational and experimental studies at supersonic Mach numbers have often reported Reynolds stress tensors with dominant streamwise contributions, this being an effect typically attributed to convective non-linearities and molecular transport.[49] Whether these discrepancies subside or persist at hypersonic Mach numbers is an open question of research.

The theoretical results provided here indicate amplified levels of post-shock fluctuation energies that could perhaps be unexpected at first, because of the high post-shock temperatures prevailing at hypersonic Mach numbers. These findings would greatly benefit from comparisons with simulations and experiments in future studies.

This theory could be extended to include additional phenomena such as: (a) non-equilibrium vibrational relaxation and finite-rate dissociation;[16,77–79] (b) multi-component gas mixtures (particularly O_2 and N_2 for shock/turbulence interactions in air); (c) compressibility and anisotropy in the pre-shock turbulence; (d) the effects of walls

downstream of the shock to address modal resonance in high-temperature inviscid shock layers around hypersonic projectiles; and (e) electronic excitation, radiation, and ionization in the post-shock gas for hypersonic flows at orbital stagnation enthalpies.

DATA AVAILABILITY

The data that support the findings of this study are available from the corresponding author upon reasonable request.

REFERENCES

[1]J. Raymond, "Shock waves in the interstellar medium," Astrophys. J. Suppl. Ser. **39**, 1 (1979).

[2]J. Dove, A. Rusk, P. Cribb, and P. Martin, "Excitation and dissociation of molecular hydrogen in shock waves at interstellar densities," Astrophys. J. **318**, 379 (1987).

[3]B. T. Draine and C. F. McKee, "Theory of interstellar shocks," Annu. Rev. Astron. Astrophys. **31**, 373 (1993).

[4]G. Bisnovatyi-Kogan and S. Silich, "Shock-wave propagation in the nonuniform interstellar medium," Rev. Mod. Phys. **67**, 661 (1995).

[5]R. Fernández and C. Thompson, "Stability of a spherical accretion shock with nuclear dissociation," Astrophys. J. **697**, 1827 (2009).

[6]R. Fernández and C. Thompson, "Dynamics of a spherical accretion shock with neutrino heating and alpha-particle recombination," Astrophys. J. **703**, 1464 (2009).

[7]C. Huete, E. Abdikamalov, and D. Radice, "The impact of vorticity waves on the shock dynamics in core-collapse supernovae," Mon. Not. R. Astron. Soc. **475**, 3305 (2018).

[8]C. Huete, F. Cobos-Campos, E. Abdikamalov, and S. Bouquet, "Acoustic stability of nonadiabatic high-energy-density shocks," Phys. Rev. Fluids **5**, 113403 (2020).

[9]V. Goncharov, O. Gotchev, E. Vianello, T. Boehly, J. Knauer, P. McKenty, P. Radha, S. Regan, T. Sangster, S. Skupsky *et al.*, "Early stage of implosion in inertial confinement fusion: Shock timing and perturbation evolution," Phys. Plasmas **13**, 012702 (2006).

[10]R. Betti and O. Hurricane, "Inertial-confinement fusion with lasers," Nat. Phys. **12**, 435 (2016).

[11]V. Tikhonchuk, "Progress and opportunities for inertial fusion energy in Europe," Philos. Trans. R. Soc. A **378**, 20200013 (2020).

[12]A. Munafò, A. Alberti, C. Pantano, J. Freund, and M. Panesi, AIAA Paper No. 2018-0171, 2018.

[13]J. MacArt, J. Wang, P. Popov, and J. Freund, "Detailed simulation of laser-induced ignition, spherical-flame acceleration, and the origins of hydrodynamic instability," Proc. Combust. Inst. **38**, 2341 (2021).

[14]J. Urzay, "Supersonic combustion in air-breathing propulsion systems for hypersonic flight," Annu. Rev. Fluid Mech. **50**, 593 (2018).

[15]G. V. Candler, "Rate effects in hypersonic flows," Annu. Rev. Fluid Mech. **51**, 379 (2019).

[16]C. Park, *Nonequilibrium Hypersonic Aerothermodynamics* (Wiley, 1990).

[17]W. Stillwell, "X-15 research results," Report No. NASA-SP60, 1965.

[18]J. Urzay and M. Di Renzo, "Engineering aspects of hypersonic turbulent flows at suborbital enthalpies," Annual Research Briefs, Center for Turbulence Research, Stanford University (2020), p. 7.

[19]M. Di Renzo and J. Urzay, "Direct numerical simulation of a hypersonic transitional boundary layer at suborbital enthalpies," J. Fluid Mech. **912**, A29 (2021).

[20]S. P. Schneider, "Effects of high-speed tunnel noise on laminar-turbulent transition," J. Spacecr. Rockets **38**, 323 (2001).

[21]D. Dolling and C. Or, "Unsteadiness of the shock wave structure in attached and separated compression ramp flows," Exp. Fluids **3**, 24 (1985).

[22]A. J. Smits and K.-C. Muck, "Experimental study of three shock wave/turbulent boundary layer interactions," J. Fluid Mech. **182**, 291 (1987).

[23]J. Andreopoulos and K. Muck, "Some new aspects of the shock-wave/boundary-layer interaction in compression-ramp flows," J. Fluid Mech. **180**, 405 (1987).

[24]Y. Zhao, S. Yi, L. He, Z. Cheng, and L. Tian, "The experimental study of interaction between shock wave and turbulence," Chin. Sci. Bull. **52**, 1297 (2007).

[25]X. I. Yang, J. Urzay, S. T. Bose, and P. Moin, "Aerodynamic heating in wall-modeled large-eddy simulation of high-speed flows," AIAA J. **56**, 731 (2018).

[26]P. S. Volpiani, M. Bernardini, and J. Larsson, "Effects of a nonadiabatic wall on supersonic shock/boundary-layer interactions," Phys. Rev. Fluids **3**, 083401 (2018).

[27]P. S. Volpiani, M. Bernardini, and J. Larsson, "Effects of a nonadiabatic wall on hypersonic shock/boundary-layer interactions," Phys. Rev. Fluids **5**, 014602 (2020).

[28]D. Sun, Q. Guo, C. Li, and P. Liu, "Direct numerical simulation of effects of a micro-ramp on a hypersonic shock wave/boundary layer interaction," Phys. Fluids **31**, 126101 (2019).

[29]W.-Z. Xie, S.-Z. Yang, C. Zeng, K. Liao, R.-H. Ding, L. Zhang, and S. Guo, "Improvement of the free-interaction theory for shock wave/turbulent boundary layer interactions," Phys. Fluids **33**, 075104 (2021).

[30]L. Fu, M. Karp, S. T. Bose, P. Moin, and J. Urzay, "Shock-induced heating and transition to turbulence in a hypersonic boundary layer," J. Fluid Mech. **909**, A8 (2021).

[31]L. Hesselink and B. Sturtevant, "Propagation of weak shocks through a random medium," J. Fluid Mech. **196**, 513 (1988).

[32]J. Keller and W. Merzkirch, "Interaction of a normal shock wave with a compressible turbulent flow," Miner. Deposita **8**, 241 (1990).

[33]S. Barre, D. Alem, and J. Bonnet, "Experimental study of a normal shock/homogeneous turbulence interaction," AIAA J. **34**, 968 (1996).

[34]K. Inokuma, T. Watanabe, K. Nagata, A. Sasoh, and Y. Sakai, "Finite response time of shock wave modulation by turbulence," Phys. Fluids **29**, 051701 (2017).

[35]K. Inokuma, T. Watanabe, K. Nagata, and Y. Sakai, "Statistics of overpressure fluctuations behind a weak shock wave interacting with turbulence," Phys. Fluids **31**, 085119 (2019).

[36]S. Lee, S. K. Lele, and P. Moin, "Interaction of isotropic turbulence with shock waves: Effect of shock strength," J. Fluid Mech. **340**, 225 (1997).

[37]K. Mahesh, S. K. Lele, and P. Moin, "The influence of entropy fluctuations on the interaction of turbulence with a shock wave," J. Fluid Mech. **334**, 353 (1997).

[38]J. Larsson and S. K. Lele, "Direct numerical simulation of canonical shock/turbulence interaction," Phys. Fluids **21**, 126101 (2009).

[39]J. Larsson, I. Bermejo-Moreno, and S. K. Lele, "Reynolds- and Mach-number effects in canonical shock–turbulence interaction," J. Fluid Mech. **717**, 293 (2013).

[40]K. Sinha, "Evolution of enstrophy in shock/homogeneous turbulence interaction," J. Fluid Mech. **707**, 74 (2012).

[41]J. Ryu and D. Livescu, "Turbulence structure behind the shock in canonical shock–vortical turbulence interaction," J. Fluid Mech. **756**, R1 (2014).

[42]R. Quadros, K. Sinha, and J. Larsson, "Turbulent energy flux generated by shock/homogeneous-turbulence interaction," J. Fluid Mech. **796**, 113 (2016).

[43]D. Livescu and J. Ryu, "Vorticity dynamics after the shock–turbulence interaction," Shock Waves **26**, 241 (2016).

[44]Y. P. M. Sethuraman, K. Sinha, and J. Larsson, "Thermodynamic fluctuations in canonical shock–turbulence interaction: Effect of shock strength," Theor. Comput. Fluid Dyn. **32**, 629 (2018).

[45]Y. Tian, F. A. Jaberi, and D. Livescu, "Density effects on post-shock turbulence structure and dynamics," J. Fluid Mech. **880**, 935 (2019).

[46]C. H. Chen and D. A. Donzis, "Shock–turbulence interactions at high turbulence intensities," J. Fluid Mech. **870**, 813 (2019).

[47]Y. P. M. Sethuraman and K. Sinha, "Effect of turbulent Mach number on the thermodynamic fluctuations in canonical shock-turbulence interaction," Comput. Fluids **197**, 104354 (2020).

[48]K. Tanaka, T. Watanabe, and K. Nagata, "Statistical analysis of deformation of a shock wave propagating in a local turbulent region," Phys. Fluids **32**, 096107 (2020).

[49]N. E. Grube and M. P. Martín, "Reynolds stress anisotropy in shock/isotropic turbulence interactions," J. Fluid Mech. **913**, A19 (2021).

[50]B. McManamen, D. Donzis, S. North, and R. Bowersox, "Velocity and temperature fluctuations in a high-speed shock–turbulence interaction," J. Fluid Mech. **913**, A10 (2021).

[51]S. Lee, S. K. Lele, and P. Moin, "Direct numerical simulation of isotropic turbulence interacting with a weak shock wave," J. Fluid Mech. **251**, 533 (1993).

[52]F. Ducros, V. Ferrand, F. Nicoud, C. Weber, D. Darracq, C. Gacherieu, and T. Poinsot, "Large-eddy simulation of the shock/turbulence interaction," J. Comput. Phys. **152**, 517 (1999).

[53]N. Braun, D. Pullin, and D. Meiron, "Large eddy simulation investigation of the canonical shock–turbulence interaction," J. Fluid Mech. **858**, 500 (2019).

[54]K. Sinha, K. Mahesh, and G. V. Candler, "Modeling shock unsteadiness in shock/turbulence interaction," Phys. Fluids **15**, 2290 (2003).

[55]B. Morgan, K. Duraisamy, N. Nguyen, S. Kawai, and S. Lele, "Flow physics and RANS modelling of oblique shock/turbulent boundary layer interaction," J. Fluid Mech. **729**, 231 (2013).

[56]H. S. Ribner, NACA Report No. 1164, 1954.

[57]H. S. Ribner, NACA Report No. 1233, 1954.

[58]H. S. Ribner, "Spectra of noise and amplified turbulence emanating from shock-turbulence interaction," AIAA J. **25**, 436 (1987).

[59]L. S. Kovasznay, "Turbulence in supersonic flow," J. Aeronaut. Sci. **20**, 657 (1953).

[60]J. Wouchuk, C. H. R. de Lira, and A. Velikovich, "Analytical linear theory for the interaction of a planar shock wave with an isotropic turbulent vorticity field," Phys. Rev. E **79**, 066315 (2009).

[61]Y. B. Zel'dovich and Y. P. Raizer, *Physics of Shock Waves and High-Temperature Hydrodynamic Phenomena* (Dover Publications, 2002).

[62]C. E. Treanor and P. V. Marrone, "Effect of dissociation on the rate of vibrational relaxation," Phys. Fluids **5**, 1022 (1962).

[63]C. H. Kruger and W. Vincenti, *Introduction to Physical Gas Dynamics* (John Wiley and Sons, 1965).

[64]S. Gordon and B. J. McBride, NASA Reference Publication No. 19950013764, 1994, p. 1311.

[65]B. J. McBride, *NASA Glenn Coefficients for Calculating Thermodynamic Properties of Individual Species* (National Aeronautics and Space Administration, John H. Glenn Research Center, 2002).

[66]N. M. Kuznetsov, "Stability of shock waves," Sov. Phys. Usp. **32**, 993 (1989).

[67]R. Menikoff and B. J. Plohr, "The Riemann problem for fluid flow of real materials," Rev. Mod. Phys. **61**, 75 (1989).

[68]J. J. Erpenbeck, "Stability of step shocks," Phys. Fluids **5**, 1181 (1962).

[69]L. Landau and E. Lifshitz, *Fluid Mechanics* (U.S.S.R. Academy of Sciences, New York, 1959), p. 61.

[70]D. Davies, "Shock waves in air at very high pressures," Proc. Phys. Soc. **61**, 105 (1948).

[71]M. Kamel, A. Ghoniem, M. Rashed, and A. Oppenheim, "Blast waves in real gases," Acta Astron. **4**, 439 (1977).

[72]S. Zhang, K. P. Driver, F. Soubiran, and B. Militzer, "Equation of state and shock compression of warm dense sodium—A first-principles study," J. Chem. Phys. **146**, 074505 (2017).

[73]N. Wetta, J.-C. Pain, and O. Heuzé, "D'yakov-Kontorovitch instability of shock waves in hot plasmas," Phys. Rev. E **98**, 033205 (2018).

[74]B.-T. Chu and L. S. Kovásznay, "Non-linear interactions in a viscous heat-conducting compressible gas," J. Fluid Mech. **3**, 494 (1958).

[75]C. Huete, T. Jin, D. Martínez-Ruiz, and K. Luo, "Interaction of a planar reacting shock wave with an isotropic turbulent vorticity field," Phys. Rev. E **96**, 053104 (2017).

[76]J. Urzay, N. Kseib, D. F. Davidson, G. Iaccarino, and R. K. Hanson, "Uncertainty-quantification analysis of the effects of residual impurities on hydrogen–oxygen ignition in shock tubes," Combust. Flame **161**(1), 1 (2014).

[77]J. W. Streicher, A. Krish, R. K. Hanson, K. M. Hanquist, R. S. Chaudhry, and I. D. Boyd, "Shock-tube measurements of coupled vibration–dissociation time-histories and rate parameters in oxygen and argon mixtures from 5000 K to 10 000 K," Phys. Fluids **32**, 076103 (2020).

[78]P. M. Finch, J. Girard, C. Strand, W. Yu, J. Austin, H. Hornung, and R. K. Hanson, AIAA Paper No. 2020-3714, 2020.

[79]J. W. Streicher, A. Krish, and R. K. Hanson, "Coupled vibration-dissociation time-histories and rate measurements in shock-heated, nondilute O_2 and O_2–Ar mixtures from 6000 to 14 000 K," Phys. Fluids **33**, 056107 (2021).